Crystallization of primitive basaltic magmas at crustal pressures and genesis of the calc-alkaline igneous suite: experimental evidence from St Vincent, Lesser Antilles arc

Michel Pichavant, Ray Macdonald

Crystallization of primitive basaltic magmas at crustal pressures and genesis of the calc-alkaline igneous suite: experimental evidence from St Vincent, Lesser Antilles arc

M. Pichavant[1] and R. Macdonald[2]

(1) Institut des Sciences de la Terre d'Orléans (ISTO), UMR 6113 CNRS-UO, 1A rue de la Férollerie, 45071 Orléans, France
(2) Environmental Centre, Lancaster University, Lancaster, LA1 4YQ, UK
M. Pichavant : Email: pichavan@cnrs-orleans.fr

Abstract

Near-liquidus crystallization experiments have been carried out on two basalts (12.5 and 7.8 wt% MgO) from Soufriere, St Vincent (Lesser Antilles arc) to document the early stages of differentiation in calc-alkaline magmas. The water-undersaturated experiments were performed mostly at 4 kbar, with 1.6 to 7.7 wt% H_2O in the melt, and under oxidizing conditions (ΔNNO = −0.8 to +2.4). A few 10 kbar experiments were also performed. Early differentiation of primitive, hydrous, high-magnesia basalts (HMB) is controlled by ol + cpx + sp fractionation. Residual melts of typical high-alumina basalt (HAB) composition are obtained after 30–40% crystallization. The role of H_2O in depressing plagioclase crystallization leads to a direct relation between the Al_2O_3 content of the residual melt and its H_2O concentration, calibrated as a geohygrometer. The most primitive phenocryst assemblage in the Soufriere suite ($Fo_{89.6}$ olivine, Mg-, Al- and Ti-rich clinopyroxene, Cr–Al spinel) crystallized from near-primary (Mg# = 73.5), hydrous (~5 wt% H_2O) and very oxidized (ΔNNO = +1.5–2.0) HMB liquids at middle crustal pressures and temperatures from □1,160 to ~1,060°C. Hornblende played no role in the early petrogenetic evolution. Derivative HAB melts may contain up to 7–8 wt% dissolved H_2O. Primitive basaltic liquids at Soufriere, St Vincent, have a wide range of H_2O concentrations (2–5 wt%).

Introduction

Arc magmatism is the key to understanding the formation of continents and the recycling of material into the mantle. High-magnesia basalts (HMB, MgO > 10 wt%) form an important, though volumetrically subordinate, proportion of arc volcanic rocks (e.g., Nye and Reid *1986*; Eggins *1993*; Rohrbach et al. *2005*). They possibly represent the primitive, mantle-derived, magmas from which the more evolved members of the arc sequence (high-alumina basalt–basaltic andesite–andesite–dacite–rhyolite) are derived by fractional crystallization ± assimilation ± magma mixing (e.g., Brophy *1989*). They also constitute valuable sources of information on the conditions of partial melting, volatile content and thermal structure of the mantle wedge (Pichavant et al. *2002a*).

The derivation of the low-MgO (MgO < 5 wt%) high-alumina basalts (HAB) typical of magmatic arcs by fractional crystallization of (near-) primary HMB has been addressed in several studies. Early experiments, performed under anhydrous conditions (Tatsumi et al. *1983*; Gust and Perfit *1987*; Ulmer *1989*; Bartels et al. *1991*; Draper and Johnston *1992*), produced derivative melts resembling HAB, although significant differences with natural compositions were noted (e.g., Draper and Johnston *1992*). Sisson and Grove (*1993a*, *b*) clearly showed that the derivation of HAB-like residual melts from more primitive basaltic

parents requires hydrous conditions. However, their experiments were performed at pressures of 1 and 2 kbar. Crystallization of arc basalts may not be restricted to such shallow depths: the generation of HAB has been commonly placed at moderate to high pressure, i.e., in the 8–10 kbar range (e.g., Gust and Perfit *1987*). Therefore, there is a need to examine the crystallization of HMB in the presence of water at pressures above 2 kbar. Grove et al. (*2003*) investigated the phase relations of primitive (MgO > 9 wt%) basaltic andesite and andesite from Mt. Shasta under water-saturated conditions at 2 and 8 kbar. A further drawback of some recent papers reporting experimental data for subduction-related HMB at high pressures has been that fO_2 has been unknown or poorly constrained (Bartels et al. *1991*; Draper and Johnston *1992*; Baker et al. *1994*), or fixed at values too low for the likely crystallization conditions of arc rocks (0 < NNO < 2; Gill *1981*; Eggins *1993*; Arculus *1994*; Brandon and Draper *1996*). Here, we report hydrous crystallization experiments on two primitive basalts from the Lesser Antilles arc, including a HMB, at 4 and 10 kbar, and attempt to constrain the melt water content and fO_2 conditions under which fractionation to HAB can proceed.

The Lesser Antilles island arc shows an unusual diversity of mafic eruptive rocks, from island arc tholeiites through calc-alkaline basalts to alkali basalts (Macdonald et al. *2000*; Pichavant and Macdonald *2003*). The Soufriere volcano of St Vincent is composed of calc-alkaline basalts and basaltic andesites (Heath et al. *1998*; Pichavant and Macdonald *2003*; Fig. 1). This volcano is also known for the frequent occurrence of gabbroic cumulate blocks (e.g., Lewis *1973a*, *b*; Arculus and Wills *1980*; Heath et al. *1998*), attesting to the extensive crystallization of basaltic magmas at depth. The most primitive magmas of the Soufriere suite are represented by olivine + spinel − phyric HMB. Pichavant et al. (*2002a*) have shown that these magmas are primary, being at equilibrium on their liquidus with a spinel lherzolite mineral assemblage for a fO_2 between NNO + 1.5 and NNO + 2.3. Multiple saturation with a lherzolitic mineral phase assemblage occurred at around 1,235°C, 11.5 kbar, for a melt with 1.5 wt% H_2O, and at around 1,185°C, 16 kbar, for a melt with 4.5 wt% H_2O. The Soufriere rocks offer, therefore, an excellent opportunity to test experimentally the crystallization behaviour of hydrous HMB at crustal pressures and, in particular, to test whether the associated HAB can be derived from HMB parents by fractional crystallization. In the context of the Lesser Antilles arc, the demonstration that HAB and HMB are genetically related would strengthen models of magma generation based on a single, although compositionally variable, mantle source, rather than on multiple sources occurring at different levels in the mantle wedge (Westercamp *1988*).

Experimental methods

Starting samples

Two samples from the Soufriere volcano of St Vincent were investigated in this study. One (STV301) is representative of HMB erupted during the early activity of the volcano (Pre-Somma lavas, Heath et al. *1998*; Fig. 1b). It typifies primitive lavas from the southern part of the Lesser Antilles arc (e.g., Arculus *1976*; Westercamp *1988*; Smith et al. *1996*; Macdonald et al. 2000; Pichavant and Macdonald *2003*). The other (STV315), also a Pre-Somma lava, is compositionally intermediate between Soufriere HMB and basaltic andesites (Fig. 1b). It may represent a composition along the calc-alkaline fractionation trend starting from HMB. The two samples are more primitive than mafic lavas or enclaves from recent eruptions along the arc (Fig. 1b). Recent experimental work on Lesser Antilles volcanic products has concentrated on andesite (Barclay et al. *1998*; Martel et al. *1998*; *1999*; Rutherford and Devine *2003*; Poussineau *2005*), more rarely on basaltic andesite (Pichavant et al. *2002b*).

The melting phase relations of primitive lavas from Grenada have been investigated at $P < 5$ kbar in the presence of water (Cawthorn et al. *1973*; Graham *1981*), and the liquidus phase relationships of STV301 have been examined at upper mantle pressures (Pichavant et al. *2002a*).

Modal data, chemical compositions and norms for the two starting samples are given in Table 1, and representative electron microprobe analyses of phenocrysts are detailed in Table 2. STV301 is representative of the most primitive rocks of the Soufriere suite (Mg# = 77, calculations at NNO + 1, Kress and Carmichael *1991*). It contains phenocrysts of olivine (ol, $Fo_{69.3–89.4}$), spinel (sp, Cr# = 50–72) and clinopyroxene (cpx, Mg# up to 90, Table 2). Our interpretation of the textural relationships is that this rock is close to the point where clinopyroxene became a coprecipitating phase with olivine and spinel. STV315 is more evolved (Mg# = 69 at NNO + 1). Together with olivine ($Fo_{75.4–88.5}$), spinel (Cr# up to 84) and clinopyroxene (Mg# = 70–78), plagioclase ($An_{54–94}$) is an important phenocryst phase and orthopyroxene (opx, Mg# = 67–72) had just joined the phenocryst assemblage (Table 2).

Experimental strategy and parameters

Near-liquidus experiments were performed on STV301 and STV315 in the presence of added water. Barometric estimates for gabbroic cumulates from the Lesser Antilles, including cumulates from St Vincent, have yielded a wide range of pressures, between 4 and 10 kbar (Arculus and Wills *1980*), indicating crystallization of basaltic liquids at middle to lower crustal depths. In this study, most experiments have been carried out at 4 kbar, mainly because the equipment employed at this pressure allows (1) fast quench rates and (2) a sensitive adjustment of experimental fO_2. Our aim was to adjust fO_2 at or slightly above the NNO buffer, in agreement with the available estimates of redox conditions for Soufriere rocks (Heath et al. *1998*). Exploratory experiments were also conducted at 10 kbar. Although the equipment used at this pressure did not allow rapid quench and fine fO_2 adjustments, one experiment is reported in this paper, to contrast the type of phase assemblages observed at 10 kbar (amphibole present) from those documented at 4 kbar (amphibole absent).

Estimates of magmatic water contents in Soufriere St Vincent basalts have yielded conflicting results. On one hand, the high Wo contents of clinopyroxene phenocrysts (Heath et al. *1998*) and the presence of amphibole in gabbroic cumulates (Arculus and Wills *1980*) are consistent with melt H_2O concentrations >5–6 wt%. On the other hand, glass inclusion studies (summarized in Heath et al. *1998*; Pichavant et al. *2002a*), pseudo-ternary diagrams (Heath et al. *1998*), high pressure phase equilibria (Pichavant et al. *2002a*) and phenocryst assemblages (relatively early appearance of plagioclase and presence of orthopyroxene in basalts, Heath et al. *1998*) suggest melt H_2O concentrations of 2–4 wt% maximum. Accordingly, H_2O was added so as to generate concentrations <6 wt% melt H_2O in most experimental 4 kbar charges, the 10 kbar charges being distinctly more hydrous (melt H_2O concentrations ~10 wt%).

Charges, containers and equipment

About 8 g of each crushed rock (grain size □50 μm) was fused twice for ≥3 h at 1,400°C in air in Pt crucibles and with grinding in between. The glasses were ground to around 20 μm. Electron microprobe analyses of the glasses are in good agreement with the XRF whole-rock data (Table 1). All experiments used these glasses as starting materials and were thus crystallization experiments.

Charges consisted of about 20–30 mg (exceptionally 50 mg) of finely ground glass plus added water. For each experiment, 3–4 charges differing in the mass of added water were prepared for each starting material. Therefore, the melt H_2O content was the main experimental parameter. Water (distilled and deionised) was added with a microsyringe. Melt H_2O concentrations (Table 3) are lower than saturation values for the melt composition and *P* and *T* of interest (Burnham *1979*). Therefore, no vapour phase was present in the charges and all experiments are H_2O-undersaturated ($aH_2O < 1$, Table 3).

Charges were loaded in containers made either of Au (run 4) or, for temperatures above 1050°C, Ag70Pd30 (runs 3, 6, 7, 1, Table 3) tubing. Pt was used for one charge (run 1, Table 3). Container capsules (20 mm length, 2.5 mm internal diameter and 0.2 mm wall thickness) were welded shut. After welding the capsules were checked for leaks by immersion in an oil bath at 120°C and then weighed. They were placed in an oven for several hours before each run to distribute the water evenly in the capsules.

All experiments were performed at ISTO, Orléans, using two internally heated pressure vessels working vertically. The 4 kbar experiments used Ar-H2 mixtures as pressurising media, obtained by sequential loading of H_2 and Ar at room temperature (Scaillet et al. *1992*). An initial H_2 pressure of around 2 bar was applied, followed by an Ar pressure of around 2 kbar. Total pressure was recorded by a transducer calibrated against a Heise Bourdon tube gauge (uncertainty ± 40 bar, including daily fluctuations). A double winding furnace assembly was used, consisting of a main Kanthal furnace and an auxiliary Pt furnace placed within each other (Roux et al. *1994*). Temperature was measured using three thermocouples (either type S or K) and recorded continuously (uncertainty ± 5 °C). Near isothermal conditions in the 2–3 cm long hot spot were obtained (gradient < 5°C/cm). The 10 kbar experiment was pressurized with pure Ar. Total pressure was recorded by a transducer calibrated against a Heise Bourdon tube gauge (uncertainty ±100 bar, including daily fluctuations). A double winding Kanthal furnace assembly was used. Temperature was measured using four type K thermocouples and recorded continuously (uncertainty ±5°C). Thermal gradients were <2°C/cm.

Run durations ranged between 13 and 25 h, around 20 h on average. The 4 kbar experiments were all rapid-quenched by using a drop-quench device, modified after Roux and Lefèvre (*1992*). Experimental capsules plus the fH_2 sensor capsule were placed together in a thin alumina tube that served as a sample holder. The alumina tube was hung in the furnace hot spot by a thin (0.2 mm) Pt wire. At the end of the experiment, the Pt wire was fused electrically, allowing the sample holder to fall into the cold part of the vessel. With this device, nearly isobaric quench rates of ~100°C/s were achieved (Di Carlo et al. *2006*). The 10 kbar experiment was quenched by switching off the power supply, resulting in a quench rate of □100–200°C/min (Prouteau and Scaillet *2003*).

Control of redox conditions

Each experiment included a Ni–Pd–O sensor capsule, which served to determine the ambient fH_2. These consisted of two pellets of NiPd metal mixtures (each with different Ni/Pd ratio) plus NiO, placed in a Pt capsule in the presence of excess H_2O (Taylor et al. *1992*). Analysis of the composition of the metal phase after the experiment allows the fO_2 of the sensor system to be determined (Pownceby and O'Neill *1994*). The fH_2 of the sensor (and by inference of the experiment since fH_2 is identical for all capsules) is then obtained from the water

dissociation equilibrium, using the fO_2 determined above, the dissociation constant of water (Robie et al. *1979*) and the fugacity of pure water at the experimental *P* and *T* (Holloway *1987*). Table 3 lists sensor compositions (mole fraction of Ni in the metallic phase, X_{Ni}) and the corresponding fH_2 of each experiment.

For a given experiment (i.e. constant *P*–*T*-fH_2), the fO_2 of each individual charge is not constant but varies along with aH_2O. The latter was determined for each charge from the H_2O content of the quenched glass, using the thermodynamic model for H_2O solution in multicomponent melts of Burnham (*1979*). The oxygen fugacity of each charge was then calculated from the water dissociation equilibrium, using the fH_2 and fH_2O determined above, and the dissociation constant of water (Robie et al. *1979*). The uncertainty on log fO_2 is less than 0.25 log units (e.g., Scaillet et al. *1995*; Martel et al. *1999*; Scaillet and Evans *1999*; Costa et al. *2004*; Di Carlo et al. *2006*). In this study, fO_2 values (Table 3) are expressed as deviations from the NNO buffer (ΔNNO values), calculated at the *P* and *T* of interest.

Analytical methods

All run products were studied petrographically and examined by scanning electron microscopy (SEM). Two Cameca electron microprobes at the Service Commun BRGM-CNRS-UO, Orléans, were used for determining the composition of starting glasses and experimental phases. Typical analytical conditions were 15 kV (acceleration voltage), 6 nA (sample current), 6–10 s (counting time on peak) and 1–2 μm (beam size). For glass analyses, the beam was defocussed to 8–10 μm. For metallic sensor phases, the acceleration voltage was 20 kV and the sample current 20 nA. Silicate and oxide standards, and ZAF and PAP correction procedures were used. Analytical uncertainties are estimated at 2% for SiO_2, Al_2O_3 and CaO, 3% for FeO, MgO and TiO_2, and 5% for MnO, Na_2O and K_2O. Mass-balance calculations were performed for each charge, using a linear algorithm adapted from Albarède (*1995*). Concentrations of all major oxides (except Cr_2O_3, MnO and H_2O) were simultaneously mass-balanced between all phases present, using the composition of starting glasses and experimental phases as input parameters. The phase proportions, bulk composition and sum of residuals (ΣR^2) were computed, the calculated FeO_t concentration (FeOcalc, Table 3) serving to estimate the amount of Fe loss.

The H_2O concentration of three experimental glasses (6–1, 7–2, 7–3, Table 3) was measured with the Cameca IMS-3F ion microprobe of CRPG, Nancy, using procedures described by Pichavant et al. (*2002a*). One glass (7–4, Table 3) was analyzed for H_2O by Karl Fischer titration (KFT) at ISTO, Orléans (Pichavant et al. *2002b*). For the other experimental glasses, the H_2O content was estimated by electron microprobe using the by-difference method (Devine et al. *1995*; Di Carlo et al. *2006*). Glasses of known H_2O concentrations (i.e., the starting glasses and those analyzed by SIMS and KFT) were used as secondary standards. These served to calibrate, for each electron microprobe session, the H_2O concentration of the glass as a function of the difference between 100% and the glass major element analytical totals. Standard deviations of glass analytical totals indicates that H_2O with this method is determined with an uncertainty <0.6 wt% (13 charges), and between 0.8 and 1 wt% (four charges).

Experimental results

A total of 22 experimental charges are reported on Table 3, 11 for STV301 and 11 for STV315. At 4 kbar, the experiments cover a temperature range from 1,200 to 1,050°C. Melt H_2O concentrations range between 1.7 and 7.7 wt% H_2O for STV301, and between 1.6 and 5.1 wt% H_2O for STV315. The experimental fO_2 range is identical for the two starting samples (ΔNNO = − 0.8 to +2.4; Table 3). The 10 kbar experiment was performed at a temperature near 1,050°C (run 1), thus allowing direct comparison with the 4 kbar, 1,050°C, experiment (run 4). However, the two 10 kbar charges are more H_2O-rich (9.4 and 9.7 wt% for STV301 and STV315 respectively, Table 3) than the 4 kbar charges.

Phase assemblages and quench crystallization

Olivine, clinopyroxene, amphibole, plagioclase and magnetite occur as stable phases in both the STV301 and STV315 charges (Table 3). Olivine forms large crystals (>100 μm) at high temperatures (T > 1,150°C), while, at lower temperatures (run 4, 1,050°C, Table 3), it tends to be smaller and/or have an irregular, rounded/embayed shape. Clinopyroxene usually occurs as small, numerous equant crystals, typically 10–15 μm in size. Amphibole (10 kbar experiment only) crystallizes to abundant euhedral prismatic phases of around 20 μm. Plagioclase is usually 5–10 μm in size, difficult to distinguish optically from the glass, and its presence was ascertained from SEM imaging. Magnetite was found only in the two 10 kbar charges (Table 3). Cr-spinel, exclusive to the STV301 charges, crystallizes to grains up to 10 μm at 1,200°C. At lower temperatures, its size reduces to 1–2 μm and detailed SEM examination is necessary to confirm its presence in run products. Orthopyroxene, present in three STV315 charges only, forms euhedral prisms larger (20–30 μm) than clinopyroxene.

Despite the use of the rapid-quench device in the 4 kbar experiments, quench phases were recognized by SEM in more than half of the charges (Table 3). At high temperature, small (1–5 μm) amphibole crystals nucleate around Cr-spinel (STV301 charges 7-2, 7-3, Table 3), the proportion of quench crystals increasing with the melt H_2O content, i.e., in the order 7-2 > 7-3 (Table 3). One additional 1,200°C STV301 charge, not reported in Table 3 and containing an initial amount of ~7 wt% H_2O, quenched to a fine intergrowth of 5–10 μm amphibole crystals. At lower temperatures, ~1 μm needle-like crystals are present. Nevertheless, no significant influence of quench crystallization on the composition of the melt has been detected. The very low residuals of the mass-balance calculations indicate that there is no need to include the quench phases in the chemical budgets. Fe–Mg partition coefficients between melt and olivine or pyroxenes vary significantly neither between charges with and without quench phases (compare for example the $K\mathrm{d}^{\mathrm{Fe–Mg}}_{\mathrm{ol–l}}$ between charges 3-5 and 3-6, Table 3), nor between charges with different amounts of quench phases present (compare the $K\mathrm{d}^{\mathrm{Fe–Mg}}_{\mathrm{ol–l}}$ between 7-2 and 7-3, Table 3). Overall, quench crystallization was of negligible importance in the 4 kbar experiments.

The two charges from the 10 kbar experiment totally lack textural features attributable to quench crystallization, on the basis of SEM examination. The explanation for an apparently efficient quench despite the relatively slow quench rate (see above) is probably the high SiO_2 contents of the two glasses, around 64.5 wt%, much higher than the SiO_2 contents of the 4 kbar glasses (48.7–56.5 wt%, Table 4).

Fe loss and mass-balance calculations

Fe losses range from +1% (i.e., Fe gain) to −10%, with an average of −2% for the 22 charges reported (Table 3). The highest Fe loss (−10%) is for charge 3–3 whose glass could not be reliably analyzed (composition estimated in Table 4) because of the high proportion of crystals present (61%, Table 3). The four supraliquidus charges 6–4, 7–4, 7–5 and 7–6 (STV315) have Fe losses from −4 to −7%, the average Fe loss for the STV315 4 kbar charges being −4%, slightly higher than for the STV301 4 kbar charges (−1%). This difference most probably comes from the method of calculation of Fe loss, because an increased proportion of Fe-rich phases (spinel or magnetite) is calculated to compensate for Fe loss to the capsule. Thus, any potential Fe loss in STV301 charges is hidden in increased amounts of calculated spinel, explaining why STV315 charges (which lack spinel) have slightly higher Fe losses. In other words, −4% is probably more representative of the actual Fe loss in STV301 charges than the −1% value calculated. These small deficits (< −10% except for charge 3-3) indicate that Fe loss has been successfully minimized in the 4 kbar charges.

In the two magnetite-bearing 10 kbar charges, no Fe losses were detected (Table 3). To check the possibility of underestimation of Fe loss, the proportion of magnetite was calculated by mass-balancing Cr_2O_3 between the starting glass, magnetite and the experimental glass. For the STV301 charge 1–9 (ran in Pt capsule, Table 3), the proportion of magnetite obtained (5.7%) is in agreement with that calculated with the eight major oxide algorithm (5.2%), thus suggesting no underestimation of Fe loss. For charge 1–5 (ran in AgPd capsule), a nil proportion of magnetite was obtained, the sensitivity of the glass Cr_2O_3 analyses being insufficient to detect magnetite crystallization in this low bulk Cr STV315 charge. Therefore, the possibility of a non-zero Fe loss for charge 1–5 can not be excluded.

Residuals of the mass-balance calculations (ΣR^2, Table 3) are generally very low, ranging from 0.02 to 1.04 (0.26 on average). Only three charges have $\Sigma R^2 > 0.5$ if charge 3–3 is excluded. This compares favourably with residuals from other studies (e.g., 0.02–0.13; Gaetani and Grove *1998*; 0.01 to >3, Pichavant et al. *2002a*), and indicates that constant bulk silicate compositions have been essentially maintained in the two sets of experimental charges. Residuals strongly correlate with Fe loss, thus indicating that quench crystallization is not the main factor responsible for the observed chemical dispersion.

Another oxide showing significant deficits is Na_2O, especially in charges from experiments 1, 4 and 3 (Table 3). Na_2O losses > −10% were commonly observed in the mass-balance calculations. In comparison, charges from experiments 6 and 7 yielded Na_2O losses between +2 (i.e., Na_2O gain) and −8%. Therefore, Na_2O loss appears specific to the lowest temperature, most H_2O-rich charges. These are also the charges that contain the most SiO_2-rich glasses and the lowest glass volume fractions, sometimes making necessary the use of an electron beam smaller than 10 μm. All these characteristics favour alkali migration during analysis of the glass. Consequently, Na_2O values for glasses 4–1, 4–2, 4–3, 4–5, 3–2, 3–6, 1–5 have been adjusted upwards by applying correction factors determined from the electron microprobe analysis of hydrous basaltic andesite glasses (Pichavant et al. *2002b*).

Equilibrium

All experiments from this study are of crystallization type and attainment of equilibrium has not been tested from reversals. However, several lines of evidence can be used to evaluate the approach toward equilibrium in our experiments.

1. Experimental durations (20 h on average) are in the range of previous phase equilibrium studies on hydrous basalts (Sisson and Grove *1993a*, *b*; Barclay and Carmichael *2004*; Di Carlo et al. *2006*). Phase assemblages and proportions of crystals vary in a systematic and consistent way with experimental conditions. One exception is provided by charge 4–6 (1,050°C, 2.2 wt% H_2O in glass, 23 h) which has a negative proportion of opx (Table 3), probably the result of an insufficient experimental duration.
2. Textural evidence (crystal morphologies, distribution of mineral phases) suggests no difficulty of nucleation and growth. The occurrence of quench phases indicates that, when oversaturated with mineral components, the hydrous melt readily crystallizes.
3. Crystals and glasses are compositionally homogeneous for a given charge. Standard deviations for hydrous glasses, olivines, amphiboles and plagioclases are in the same range or lower than analytical dispersions (Table 4). For pyroxenes, standard deviations for Al_2O_3, SiO_2 and MgO may slightly exceed the analytical dispersion (both pyroxenes in charge 4–6, clinopyroxene in charge 3–2, orthopyroxene in charge 3–6). Spinel is slightly heterogeneous in charge 4–3. Experimental compositions vary in a systematic and consistent way with T, H_2O melt and fO_2, except Cr–Al spinels in the low-temperature charges, as detailed below.
4. Crystal-liquid exchange coefficients (K_d) for olivine, clinopyroxene, orthopyroxene, amphibole and plagioclase (Table 3) agree with values from the literature under comparable conditions (discussed in detail below). This suggests that equilibrium phase compositions were obtained.
5. The low residuals from the mass-balance calculations and the lack of large (>−10%) Fe losses in the experiments show that bulk silicate compositions were kept essentially constant. We conclude that all experiments reported in Table 3, except probably charge 4-6, have closely approached equilibrium.

Four kilobar phase relationships

The 4 kbar phase relationships for the HMB STV301 are represented on a *T*-H_2O in melt section (Fig. 2). Spinel is present in most charges, irrespective of the phase assemblage, but absent from the two driest and most reduced charges (3-3 and 6-2, Table 3). In 6-2, a large (20 μm) grain of high-Cr spinel, with a lower-Cr rim, probably represents refractory material left after preparation of the starting glass and partially reacted during the experiment. Olivine and spinel are the liquidus phases. The phase diagram is characterized by a large primary ol field (compare Graham *1981*). At 1,200°C, the ol saturation curve is bracketed by charge 7-2 (4.7 wt% H_2O), and by the charge with 7 wt% H_2O added which could not be satisfactorily quenched but revealed that no phase other than melt was present at run conditions. Using the high pressure data of Pichavant et al (*2002a*), the ol saturation curve is constrained to be relatively flat in T-H_2O in melt space (Fig. 2). Saturation curves for the other phases are steeper, and in the order plag > cpx. These two phases co-saturate over a small temperature interval and their saturation curves are expected to cross for a melt H_2O concentration around

1.5 wt% (Fig. 2). Saturation in cpx is reached once around 12 wt% ol has crystallized, irrespective of temperature.

The T-H_2O in melt 4 kbar isobaric section for basalt STV315 has been constructed by using all the experimental data points available, including charge 4-6. Cr–Al spinel is absent, a result of the relatively low bulk Cr concentration of the starting material (Table 1). STV315 is nearly multiply saturated with respect to ol, opx, cpx and plag for H_2O in melt and temperature around 3 wt% and 1,120°C. For melt H_2O concentrations > 3 wt%, olivine is the liquidus phase, followed by cpx and plag. Saturation in cpx is reached once a maximum of 5 wt% ol has precipitated. Cpx and plag are both more abundant than ol (maximum proportion <10 wt%). For melt H_2O concentrations <3 wt%, opx replaces ol through the ol + l = opx peritectic reaction. The phase diagram is drawn with opx as the liquidus phase (Fig. 3). Opx is always subordinate in abundance to cpx and plag (charges 3-6 and 6-5, Table 3).

Ten kilobar phase relations

Results of the two 10 kbar charges (one for each starting composition) are detailed in Table 3. Both are characterized by the presence of amphibole as a major phase, with proportions exceeding 30 wt% in the STV315 and 60 wt% in the STV301 charge (Table 3). The melt at equilibrium with amphibole in the two charges is very H_2O-rich (>9 wt%; Table 3) and silicic (>64 wt% SiO_2, Table 4). Amphibole is accompanied by cpx and mt, but ol and plag are both absent. These results are consistent with previous work on amphibole crystallization in hydrous basalts (Cawthorn et al. *1973*; Holloway and Burnham *1972*; Müntener et al. *2001*; Barclay and Carmichael *2004*; Grove et al. *2003*). They provide further evidence that amphibole can reach saturation in high-MgO basalts.

The absence of amphibole in the 4 kbar phase assemblages (Table 3) underlines the marked contrast between the 4 and 10 kbar results. However, amphibole is present in STV301 experiments performed at 4 kbar, 1,000 and 1,025°C (Pichavant et al., in preparation), and is consequently a subliquidus phase at this pressure. In contrast, at 10 kbar and for our specific H_2O-rich conditions, amphibole is closer to the STV301 liquidus. Therefore, increasing pressure under near H_2O-saturated conditions stabilizes amphibole closer to the liquidus of high-MgO basaltic melts (Holloway and Burnham *1972*; Grove et al. *2003*).

Compositions of experimental crystalline phases

Olivine has Fo contents ranging from 90.5 to 75.7, generally higher in STV301 (80–90.5) than in STV315 charges (75.7–84.6, Table 4). On average, olivine contains 0.28 wt% CaO (range 0.17–0.43 wt%) and 0.25 wt% MnO (range 0.14–0.37 wt%). The olivine-liquid exchange coefficient ($K_d^{Fe–Mg}{}_{ol\text{-}l}$) is 0.32 ± 0.04 (Table 3, $n = 14$), calculated with Fe as FeO, the glass FeO being determined from Kress and Carmichael (*1991*), using data in Tables 3 and 4. This K_d is similar to those found in recent experimental studies of hydrous basaltic compositions (0.27–0.33, Sisson and Grove *1993a*; 0.31–0.32, Pichavant et al. *2002a*; 0.28 + 0.06, Barclay and Carmichael *2004*; 0.36 + 0.04, Di Carlo et al. *2006*). Olivine Fo contents systematically decrease with decreasing melt fraction and increasing ol mass fraction in the charge. Therefore, ol proportion contours (e.g., Fig. 2) are correlated to olivine Fo contours. For STV301, olivine crystallizing near the liquidus has Fo between 90 and 91 (charge 7-2, Table 4; Fig. 2). At the beginning of cpx crystallization, Fo is around 86 (charges 6-1, 3-1 and 4-1, Table 4), decreasing to 80–83 when plagioclase joins ol and cpx (charges 6-

2, 3-2, 3-3, 4-2, 4-3, Table 4). For STV315, Fo contents are around 85 for near-liquidus olivines, 84 for cotectic ol + cpx, and 80 for ol + cpx + plag (Table 4).
Clinopyroxene has Wo contents ranging from 48.5 to 31.6%, Fs from 5.4 to 14% and En from 42.8 to 54.4% (pyroxene end-members calculated with Fe = Fe^{2+}, Fe^{2+} and Fe^{3+} being computed after Lindsley *1983*). Experimental cpx is aluminous (4.92–8.32 wt% Al_2O_3), Ti-poor (0.44–1.20 wt% TiO_2) and Cr-bearing (Table 4). On average, both Al_2O_3 and TiO_2 are higher, and Cr_2O_3 lower, in STV301 than in STV315 charges. The 4 and 10 kbar cpx compositions are similar. The clinopyroxene-liquid exchange coefficient ($K_d^{Fe–Mg}{}_{cpx\text{-}l}$), calculated by averaging the data for all cpx-bearing charges, is 0.29 ± 0.08 (Table 3, n = 13, calculations performed with Fe^{2+} in clinopyroxene and with glass FeO determined from Kress and Carmichael *1991*). This K_d overlaps with those from recent experimental studies of hydrous basaltic compositions (0.25–0.28, Sisson and Grove *1993a*; 0.35 + 0.07, Di Carlo et al. *2006*).

The Ca atomic content in cpx (expressed here as Wo) progressively decreases with decreasing H_2O in the coexisting melt (see also Gaetani et al. *1993*; Di Carlo et al. *2006*). The decrease in Wo is best seen at constant temperature, for example in the 6 charges at 1,050°C, 4 kbar (run 4, Table 3). Mg# (calculated with Fe = Fe^{2+}) and $Fe^{3+}/\Sigma Fe$ (Fe = Fe^{2+}, Fe^{3+}) is positively correlated with melt H_2O content and fO_2, the highest values (Mg# = 89, $Fe^{3+}/\Sigma Fe$ = 55%) being found in the most H_2O-rich and oxidized STV301 charges at 1,050°C, 4 kbar. The 10 kbar cpx have lower Mg# and Fe^{3+}/Σ Fe than the 4 kbar, a consequence of the low glass fractions at 10 kbar.

Orthopyroxene (STV315 charges) has Fs from 17.2 to 21.8% and En from 73.6 to 77.6%. The Wo content ranges from 4.6 to 5.3%, straddling the boundary between enstatite and pigeonite. Mg# (77–82) is strongly correlated with temperature, the most magnesian opx being found at 1,150°C (charge 6-5, Tables 3, 4). Orthopyroxene has moderately high Al_2O_3 (2.17–4.66 wt%), low TiO_2 (0.2–0.32 wt%) and contains some Cr_2O_3 (0.14–0.29 wt%). The orthopyroxene-liquid exchange coefficient ($K_d^{Fe–Mg}{}_{opx–l}$), calculated as for the $K_d^{Fe–Mg}{}_{cpx\text{-}l}$ and averaging the data for the 3 opx-bearing charges (i.e., including charge 4-6), is 0.28 ± 0.02 (Table 3), similar to those found in recent experimental studies on hydrous mafic compositions (0.32 + 0.02, Gaetani and Grove *1998*; 0.34 + 0.04, Pichavant et al. *2002a*).
Amphibole is a hornblende (hb) with moderately high amounts of Al_2O_3 (Al^{IV} = 1.64–1.69 apfu), 0.79–0.83 cations pfu in site A and very elevated Mg# (0.81–0.82, calculated with FeO = FeO_t). The hornblende-liquid exchange coefficients ($K_d^{Fe–Mg}{}_{hb–l}$), calculated with FeO = FeO_t (in both hb and glass) are 0.31 and 0.38, (data in Table 4), in good agreement with values from the literature (0.30–0.38, Sisson and Grove *1993a*; 0.36, Pichavant et al. *2002b*; 0.32, Grove et al. *2003*).
Plagioclase An content ranges from 69.2 to 85.4 and Or from 0.4 to 1.4, overlapping between the two series of charges. The plagioclase-liquid Ca–Na exchange coefficient ($K_d^{Ca–Na}{}_{plag–liq}$) is strongly correlated with the H_2O content of the melt, increasing from 1.3 (1.5–2 wt% H_2O) to 4.5 (~6 wt% H_2O), in good agreement with values for basaltic compositions for comparable melt H_2O concentrations (Sisson and Grove *1993a*; Pichavant et al. *2002b*; Di Carlo et al. *2006*). Plagioclase crystallizing together with ol and cpx at 1,050°C under wet conditions (H_2O in melt = 5–6 wt%) is the most calcic (~An_{85}). At 1,150°C, and for a melt H_2O content around 2 wt%, plagioclase coexisting with either ol or opx + cpx assemblages is An_{70}.

Cr–Al spinel has a narrow range of Cr#, from 29 to 44 (Table 4). Mg# (calculated with Fe = Fe^{2+}) regularly increases with temperature, from 44 (1,050°C) to 70 (1,200°C). Both $Fe^{3+}/\Sigma R^{3+}$ (R^{3+} = Al^{3+}, Cr^{3+}, Fe^{3+}) and Fe^{3+}/Σ Fe increase with log fO_2, and good positive

correlations with ΔNNO are obtained if spinels from high-temperature (>1,150°C) experiments (Table 4; Pichavant et al. *2002a*) are plotted. Olivine-spinel equilibria (Ballhaus et al. *1991*) applied to high-temperature charges 6-1, 7-2, 7-3 yield log fO_2 slightly lower than experimental values, by 0.6, 0.3 and 0.9 log units, respectively. In contrast, when applied to the low-temperature (<1,100°C) charges 4-1, 4-2, 4-3, 3-1, 3-2, log fO_2 higher than experimental values by □2 log units are obtained. In experiments 3 and 4, spinels have low Cr contents, higher $Fe^{3+}/\Sigma R^{3+}$ and Fe^{3+}/Σ Fe for a given ΔNNO than the high-temperature spinels, and are too Cr-poor and Fe^{3+}-rich to represent equilibrium compositions. Accordingly, spinel compositions in the low-temperature experiments 3 and 4 have been corrected by increasing Cr and decreasing Fe^{3+} (at constant $Cr + Fe^{3+}$) until the calculated log fO_2 (Ballhaus et al. *1991*) becomes identical to the experimental value. In the following, only the corrected spinel compositions are used. *Magnetites* from the two 10 kbar charges are compositionally very close, with 7 wt% TiO_2, 3 wt% Al_2O_3, 3.7 wt% MgO and <1 wt% Cr_2O_3 (Table 4).

Composition of experimental glasses

The 4 kbar glasses have basaltic to basaltic andesite compositions, with a predominance of basalts in the STV301 charges (SiO_2 = 48.7 – 53.5 wt%), and of basaltic andesites in the STV315 charges (SiO_2 = 52.3–56.5 wt%, Table 4). The two 10 kbar glasses are dacitic (SiO_2 ~ 64.5 wt%). Six STV301 glasses meet the compositional criteria for arc HAB suggested by Draper and Johnston (*1992*), viz. SiO_2 from 48 to 53 wt%, Al_2O_3 > ~ 17.5 wt%, CaO > ~ 8.5 wt%, and MgO < 9 wt%. The glasses from charge 7-2 and 7-3 are HMB, according to the Draper and Johnston (*1992*) criteria, except that the TiO_2 contents (respectively 1.06 and 1.24 wt%) are higher than their suggested □0.75 wt%. Thus, the STV301 melts span the transition from HMB to HAB. Only one STV315 glass (3-5) has an HAB composition, the SiO_2 contents of glasses 4-4 and 4-5 being slightly too high to fullfill the criteria above.

Glass SiO_2, TiO_2, Al_2O_3, Na_2O and K_2O abundances increase with progressive crystallization and differentiation, while MgO, CaO and CaO/Al_2O_3 decrease. FeO_t slightly decreases during the initial stages of crystallization but shows an increase in the driest and most reduced, plagioclase-rich charges (3-6, 6-2, 6-5, Tables 3, 4). The 10 kbar glasses generally extend the trends defined by the 4 kbar glasses, except for TiO_2 and FeO_t which are strongly depleted as a result of massive (>5 wt%) magnetite crystallization in the 10 kbar charges. On the FeO_t/MgO versus SiO_2 diagram (Fig. 4), the 4 and 10 kbar glasses are dramatically separated. The STV301 and STV315 4 kbar glass trends are both slightly steeper than the tholeiitic-calc-alkaline dividing line, which has been shown to correspond, in terms of fO_2, to the NNO + 1 isobar (Pichavant et al. *2002b*, their figure 9). The STV301 and 315 trends (Fig. 4) are consistent (Pichavant et al. *2002b*) with experimental fO_2 values being slightly more reduced on average than NNO + 1 (the average Δ NNO is +0.5 for both sets of 4 kbar charges) although, in detail, fO_2 progressively decreases with crystallization, i.e., from lower to higher FeO_t/MgO (Fig. 4). In contrast, the two 10 kbar charges have very high SiO_2 and intermediate FeO_t/MgO, plotting well into the calc-alkaline field (Fig. 4). Their position is consistent with their strongly oxidizing (ΔNNO > +2) nature and specific phase assemblage (amphibole + magnetite, see Pichavant et al. *2002b*).

Glass composition is primarily controlled by the type of crystalline phase assemblage present. Using MgO as a differentiation index, glass CaO and Al_2O_3 concentrations increase linearly as a result of olivine fractionation (Fig. 5a, b). The highest CaO concentrations (12.8 and 10.9 wt% CaO for STV301 and STV315, respectively) are reached before cpx joins the

liquidus (Fig. 5a). For lower MgO concentrations, CaO drops as a result of cpx and plag crystallization. In comparison, Al_2O_3 concentrations in glasses at equilibrium with ol + cpx monotonously increase with decreasing MgO (Fig. 5b), reaching values >20 wt% Al_2O_3 for MgO <5 wt% (Fig. 5b). This provides extra evidence that the view of Crawford et al. (*1987*), that HAB never exist as liquids and form instead by plagioclase accumulation, is unjustified as a general hypothesis. The 10 kbar charges, which are plagioclase-free, have glass Al_2O_3 concentrations of ~22 wt% and □8 wt% CaO at MgO < 1 wt%. In contrast, at 4 kbar, Al_2O_3 concentrations are limited by plagioclase saturation. Since H_2O suppresses plagioclase crystallization (Figs. 2, 3), the highest glass Al_2O_3 concentrations are obtained in the most H_2O-rich charges, obtained at 1,050°C (4-2, 4-3) which contain the highest mass fractions of ol + cpx + sp at the point of plagioclase saturation (Fig. 6). Glass Al_2O_3 concentrations reach 21.0 wt% in the STV301 charges (4-3) and, in STV315, 19.1 (4-5, opx-free) and 19.2 wt% (4-6, opx-bearing). Therefore, the attainment of elevated Al_2O_3 concentrations in residual glasses requires both high melt H_2O concentrations and low temperatures.

In comparison with the 4 kbar hydrous trends from this study (see also Sisson and Grove *1993a*; Gaetani et al. *1994* for similar results at $P < 4$ kbar), glasses from the high-pressure and anhydrous crystallization of HMB (Draper and Johnston *1992*) are characterized by lower CaO at a given MgO, plotting outside the HAB field for typical MgO concentrations of 4-5 wt% (Fig. 5a). These results are the direct consequence of the respective crystallization sequences. Hydrous conditions stabilise olivine-only crystallization for a substantial temperature interval (Fig. 2), allowing Ca enrichment in residual melts. Calcic phases precipitate much earlier in high pressure and anhydrous melts (Draper and Johnston *1992*): at 10 kbar, clinopyroxene + plagioclase (+orthopyroxene) join olivine at 1,275°C and subsequent melts show Ca depletion. Macdonald et al. (2000) divided the Lesser Antilles basaltic rocks into two groups, the key compositional difference being the CaO abundances at a given MgO level. Protracted olivine-only crystallization leads to the Ca enrichment seen in the high-Ca group, represented on Fig. 5a by the STV301 4 kbar hydrous trend; early cotectic crystallization of ol + cpx (+plag) generates melts poorer in Ca (the 10 kbar and anhydrous Draper and Johnston trend on Fig. 5a).

Discussion

Hydrous basalt crystallization and genesis of the calc-alkaline suite

The earliest stage of fractionation of primitive, hydrous, low-K_2O arc basalts is dominated by crystallization of ol + sp and ol + cpx + sp. High-MgO liquids such as STV301 crystallize ol + cpx over a substantial temperature interval (Fig. 2; see also Graham *1981*; Sisson and Grove *1993a*; Gaetani et al. *1994*). In less magnesian liquids such as STV315, ol and cpx appear nearly simultaneously (Fig. 3). Plagioclase was found as a near-liquidus phase neither in STV301 nor in STV315. For H_2O concentrations above either □1.5 (STV301) or □3 (STV315) wt%, plag is the third silicate to crystallize (Fig. 2, 3). The liquid lines of descent reflect the combined effects of ol + cpx fractionation and suppression of plagioclase crystallization (e.g., Yoder *1965*; Sisson and Grove *1993a*). Residual liquids at equilibrium with ol + cpx + sp assemblages are progressively depleted in ol and cpx components, and enriched in plag (Fig. 7, 8) and qz (Fig. 8) components, essential features of the calc-alkaline differentiation trend (e.g., Grove and Baker *1984*; Gust and Perfit *1987*; Sisson and Grove *1993a*). Thus, early crystallization of ferromagnesian silicates produces compositions typical of the more evolved members of the arc sequence. The effect of H_2O on residual melt composition is directly seen at constant pressure by comparing, for STV301, charges 6-2 (1.7 wt% H_2O) with 4-3 (5.9 wt%) and, for STV315, charges 6-5 (1.6 wt%) with 4-5

(3.9 wt%, Figs. 7, 8). Saturation in plagioclase occurs at lower normative plag in glasses with low rather than high H_2O contents.

Spinel may be present during the early stages of ol + cpx fractionation, as illustrated by the STV301 charges. Fractionation of sp depletes the residual melt in FeO_t, to a lesser extent in MgO, increases SiO_2 and alkalis, and shifts the melt composition toward the calc-alkaline field (Fig. 4). The proportion of crystallizing sp exerts an important influence on the FeO_t/MgO of the melt (Fig. 4; see also Sisson and Grove *1993a*; Pichavant et al. *2002b*). Therefore, when sp is a near-liquidus phase, the compositional effects arising from the early crystallization of ferromagnesian silicates are amplified. Early crystallization of sp has been ascribed to the influence of hydrous conditions (Sisson and Grove *1993a*). However, other factors such as high fO_2 and bulk composition (in particular high Cr) may be more effective than H_2O in stabilizing spinel near the liquidus of basaltic melts. The lack of sp in the two STV301 charges 3-3 and 6-2 (which are the less oxidized of the STV301 charges) and in all STV315 charges (from a relatively low Cr bulk composition, Table 1) illustrates the importance of these two parameters.

Early hornblende crystallization will introduce major changes in the fractionation scheme above. Olivine and cpx, if present, will be resorbed (e.g., Holloway and Burnham *1972*; Barclay and Carmichael *2004*). In terms of major element fractionation, hb-bearing assemblages lead to a slight decrease of CaO, and to an increase of Al_2O_3 at decreasing MgO, similar to that observed for ol + cpx fractionation (Fig. 5). However, the SiO_2 content of the residual liquid will be much higher as a result of hb than of ol + cpx fractionation (Fig. 4). Therefore, there should be a major difference in the silica content of residual magmas depending on the fractionation scheme, respectively HAB in the case of ol + cpx fractionation and andesites or more evolved rocks in the case of hb fractionation. A comparison between the 4 and 10 kbar glasses (Fig. 4) clearly illustrates this point. However, to affect early fractionation in hydrous basaltic melts, hornblende has to be a near-liquidus phase. This requires pressures in the lower crustal/upper mantle range, elevated H_2O concentrations and appropriate melt compositions (Holloway and Burnham *1972*; Grove et al. *2003*).

The fact that opx occurs in STV315 but is absent from STV301 charges indicates compositional control on opx stability. The three opx-bearing charges have glass SiO_2 contents of 52.6, 54.6 and 56.5 wt% (Table 4). This includes the two most silica-rich among the 4 kbar glasses, and suggests that melt compositions with at least ~53 wt% SiO_2 (i.e. basaltic andesite and more evolved) are required to crystallize opx in hydrous basaltic bulk compositions. Opx appears in virtually all natural Lesser Antilles suites, at □4 wt% MgO (Macdonald et al. *2000*). However, the opx stability field is restricted to the low-H_2O in melt portion of the 4 kbar phase diagram (Fig. 3). At melt H_2O contents <3 wt%, opx appears as a reaction product between ol and melt. At higher melt H_2O contents, opx is no longer present, indicating that opx is stable only for low melt H_2O concentrations in mafic to intermediate melts (see also Sisson and Grove *1993a*; Martel et al. *1999*; Pichavant et al. *2002b*). The effect of H_2O on opx stability is, in our experiments, demonstrated at constant pressure, but not at strictly constant fO_2 since ΔNNO increases along with increasing melt H_2O content. However, Pichavant et al. (*2002b*) have shown that increasing fO_2 at constant melt H_2O concentration depresses opx stability. Therefore, both the melt H_2O content and fO_2 have the same type of influence on opx stability.

Al_2O_3 content of arc basaltic liquids

The depression of plagioclase crystallization in hydrous systems leads to an enrichment of the residual melt in Al_2O_3 (Figs. 5b, 6) and Plag components (Figs. 7, 8). Therefore, a relation between the Al_2O_3 content of the residual melt and its H_2O concentration is expected (Fig. 6). Hydrous conditions, when combined with low-temperatures, generate residual melts with high Al_2O_3 concentrations because ferromagnesian silicates and oxides may crystallize in large amounts before plagioclase starts to precipitate. We have empirically regressed the Al_2O_3 content of experimental liquids as a function of the melt H_2O concentration, temperature and melt composition, to provide a melt-based geohygrometer applicable to arc basaltic liquids (see also Sisson and Grove *1993b*).

The regression has been calibrated from a set of 34 hydrous mafic liquids mainly from low pressure experiments (32 at $P < 4$ kbar, 2 at 10 kbar). The total range of melt H_2O concentrations is 1.2–9.7 wt%, with a majority between 2 and 6 wt%. Only charges with assemblages of four and five phases have been considered to restrict the variance (Sisson and Grove *1993b*). With the exception of four charges, the database comprises only plagioclase-saturated experiments because plagioclase effectively limits the Al_2O_3 concentration in the melt (Figs. 5b, 6). Exceptions include two 4 kbar ol + cpx + sp charges close to plagioclase saturation (4-2, 3-2, Table 3) and the two 10 kbar charges from this study (1-5, 1-9, Table 3) which have been included to extend the range of melt Al_2O_3 and H_2O concentrations. Except these two 10 kbar charges, all melts in the calibrating database have $SiO_2 < 55$ wt%, $FeO_t < 10$ wt%, MgO > 3.5 wt% and $K_2O < 3.5$ wt% (anhydrous basis). The formulation of the model is given in Table 5. Pressure was not included in the regression because most calibrating experiments are <4 kbar. The regression should be seen as no more than an empirical fit of the Al_2O_3 contents of low-pressure, plagioclase-saturated, hydrous basaltic liquids as a function of temperature and melt H_2O content. The correlation coefficient (r^2) is 0.92 and the expression of Table 5 recovers the melt Al_2O_3 and H_2O concentrations of the calibrating experiments with average errors of +0.3 and +0.5 wt%, respectively.

The average of olivine-hosted glass inclusions ($SiO_2 < 54$ wt%) in the 1979 Soufriere eruption products (Devine and Sigurdsson *1983*) yields calculated melt H_2O concentrations in the range 6.1–4.0 wt% for temperatures between 950 and 1,100°C (Fig. 9). For an interstitial glass in a gabbroic cumulate (Lewis *1973a*), the calculated melt H_2O concentration is 4.6 wt% at 950°C. Values between 4.4 (1,100°C) and 6.6 (950°C) wt% H_2O are obtained for one basaltic inclusion trapped in olivine from the Kick'em Jenny submarine volcano (Devine and Sigurdsson *1995*). Representative glass inclusions from a large data set on St Vincent island (Bouvier et al., written communication 2006) yield a total range of H_2O concentrations between 4.4 and 7.5 wt% (Fig. 9). Therefore, the Al_2O_3 in melt regression establishes the presence of relatively H_2O-rich basaltic liquids at St Vincent and elsewhere in the Lesser Antilles, and in other arcs as well (Fig. 9). Note that plagioclase saturation is assumed in the calculations above. If this is not the case, then the H_2O concentrations are maximum values.

Early petrogenetic evolution of the Soufriere suite

Magmas sustaining the activity of Soufriere in the last few thousand years have dominantly been low-MgO basalts and basaltic andesites (Graham and Thirlwall *1981*; Bardintzeff *1983*; Devine and Sigurdsson *1983*; Heath et al. *1998*; Fig. 1). There is agreement that these magmas are derived from primitive basaltic parents (Graham and Thirlwall *1981*; Bardintzeff *1983*; Devine and Sigurdsson *1983*; Heath et al. *1998*). Heath et al. (*1998*) have suggested

that HMB similar to the older erupted (STV301) are parental to the recent basaltic andesites (see also Graham and Thirlwall *1981*). Below, our experimental results are combined with existing mineralogical and petrological data (Graham and Thirlwall *1981*; Marcelot et al. *1981*; Heath et al. *1998*) to constrain early differentiation in the Soufriere lavas.

Compositions of olivine from the Soufriere suite are compared with experimental olivines in Fig. 10. The natural olivines show a large variation in Fo content, from <60 to about 90. Olivines with Fo > 88 occur in lavas of various types and eruption ages (Heath et al. *1998*). In these different rock types, olivines have identical maximum Fo contents (89.4 in HMB; 89.6 in basalts; 89.7 in basaltic andesites, Marcelot et al. *1981*; Heath et al. *1998*), suggesting parental melts with constant Mg#. The occurrence of Fo-rich olivines in rocks that are too evolved on the basis of olivine-liquid equilibrium (i.e., $Fo_{88.5}$ in STV315, much higher than the maximum in experiments, $Fo_{84.6}$), suggests that primitive magmas, presumably HMB, are involved in the genesis of these rocks, and indicates transfer of phenocrysts from primitive to more evolved magmas, most probably during magma mixing.

Olivines with CaO <0.1 wt% include a primitive group with Fo up to 89.7 and Ni up to 0.38 wt% (Marcelot et al. *1981*; Heath et al. *1998*). On Fig. 10, these five compositions nearly overlap with olivines from the peridotite xenoliths of Grenada (Parkinson et al. *2003*). We interpret these ol compositions are representing crystals disaggregated from mantle rocks, presumably xenoliths, and entrained in the Soufriere magmas.

The maximum Fo in STV301 experiments (90.5) exceeds that of olivine phenocrysts (89.6). Calculated Fo of liquidus ol range between 90.3 (NNO) to 93 (NNO + 2.5), using STV301 glass composition from Table 4, $K_d^{Fe-Mg}{}_{ol-l}$ from this study and melt FeO from Kress and Carmichael (*1991*). Therefore, ol phenocryst compositions require that the parental basaltic melts at Soufriere are slightly less primitive than STV301. The composition of a parental melt has been calculated by incrementally subtracting olivine with equilibrium Fe/Mg ratio from the STV301 bulk composition until a Mg# in equilibrium with $Fo_{89.6}$ is reached. The resulting melt (PAR1, Table 1) is a HMB with a Mg# (73.5) slightly lower than STV301 (76.8 at NNO + 1).

Natural cpx have Mg# (calculated with $Fe = Fe^{2+}$) ranging from 66 to 91, mostly <80 (Graham and Thirlwall *1981*; Marcelot et al. *1981*; Heath et al. *1998*), indicating that a majority of cpx in the Soufriere suite crystallized from relatively evolved melts. Cpx in STV301 have Mg# up to 90 (Fig. 11). One critical observation is the splitting of the most magnesian (Mg# >85) natural cpx population into two compositionally distinct groups, based on their Al_2O_3 and TiO_2 (Fig. 11). The Al- and Ti-rich cpx (group 1, maximum Mg# = 90) are well matched by the experimental cpx compositions, and are interpreted as early phenocrysts from primitive basaltic liquids. In contrast, the Al- and Ti-poor compositions (group 2, maximum Mg# = 91) have not been experimentally reproduced. Both groups are Cr-rich (group 1: 0.69–0.99; group 2: 0.22–0.87 wt% Cr_2O_3), but Fe^{3+}/Σ Fe at equivalent Mg# is distinctly higher in group 1 than in group 2 cpx. Since group 2 extends to the cpx compositions in the peridotite xenoliths from Grenada (Fig. 11; Parkinson et al. *2003*), these crystals are interpreted as coming from similar peridotite xenoliths and incompletely reequilibrated in the Soufriere lavas.

Experimental charges in which the composition of magnesian group 1 cpx phenocrysts is approached constrain the composition of cotectic melts. The melt in charge 4-1 can be taken as the cotectic melt at the point of cpx saturation since that charge has the lowest proportion of cpx. From there, the composition of parental Soufriere melts can be calculated by

incrementally adding olivine with equilibrium Fe/Mg ratio to glass 4-1 until a Mg# at equilibrium with $Fo_{89.6}$ ol is reached. The parental melt obtained is again a HMB (PAR2, Table 1), slightly higher in Al_2O_3 and MgO, and lower in FeO_t and CaO than PAR1.

Soufriere spinel compositions are Cr- and Fe^{3+}-rich (Fig. 12; Marcelot et al. *1981*; Heath et al. *1998*), typical of primitive arc basalts (Arculus *1978*; Eggins *1993*). The most magnesian varieties (Mg# = 53, Cr# = 51) are similar to the less refractory spinels in the Grenada peridotite xenoliths (Parkinson et al. *2003*). Spinels from the high-temperature (>1,150°C) charges are more magnesian than spinels in the rocks, suggesting that these latter equilibrated at temperatures <1,150°C. Spinels from the low-temperature (<1,100°C) charges approach the most magnesian and aluminous spinels in STV301 (Fig. 12).

In summary, phenocrysts in the Soufriere suite include a distinctive primitive assemblage with ol ($Fo_{89.6}$), cpx (Mg# = 90) and Cr-Al sp (Mg# = 53, Cr = 51), which marks the earliest stages of magma crystallization and differentiation. The recognition of ol and cpx with typical mantle compositions links magma generation and equilibration in the mantle and the early crystallization history. Hornblende is absent as a phenocryst in the Soufriere lavas. However, it is a major phase in the gabbroic cumulates (e.g., Lewis *1973a*, *b*; Arculus and Wills *1980*). In these cumulates, hb may coexist with ol and cpx, both of relatively low Mg# (e.g., unzoned Mg# 72 hb coexisting with Fo_{76} and Mg# 84 cpx, Lewis, *1973a*, *b*), suggesting that amphibole crystallizes relatively late. Hornblendes in the cumulates have Mg# ranging from 68 to 78 with a majority in the range 70–72 (Pichavant, Maury and Macdonald, unpublished data), and thus are less magnesian than the amphiboles in the 10 kbar charges (Mg# = 81–82, Table 4). This indicates that the cumulate hornblendes crystallized from melts less primitive than STV301 and STV315. We, therefore, conclude that amphibole plays no role in the early petrogenetic evolution of the Soufriere suite, which is controlled by ol + cpx + sp fractionation.

T-H_2O-fO_2 of parental Soufriere liquids: constraints from primitive phenocrysts

In charges 4-1 and 4-2 at 1050°C (7.7 and 6.3 wt% H_2O), experimental cpx have Mg# nearly identical to the maximum of phenocrysts, whereas Al_2O_3 and TiO_2 are both slightly lower (Fig. 11). At 1,100°C (charge 3-2, 4.2 wt% H_2O), experimental cpx has slightly higher Al_2O_3 and TiO_2 but lower Mg# than the most magnesian phenocryst. Additional constraints on melt H_2O content and pressure are obtained from Al^{VI} in cpx (Fig. 14). The Al^{VI} of the most magnesian cpx phenocryst is bracketed by charges 4-1 and 4-2, on one hand, and 3-2 on the other (Fig. 14). Therefore, this cpx crystallized from melts containing 5–6 wt% H_2O at 1,060°C (Fig. 11). Although precise constraints on pressure are lacking, the low Al^{VI} of primitive cpx phenocrysts rule out crystallization at pressures >10 kbar (Fig. 14). The data at 4 kbar reproduce satisfactorily the compositional characteristics of these primitive cpx and we conclude that they crystallized in the middle crust.

Since ol is the liquidus phase for parental melts PAR1 and PAR2, olivine crystallization must necessarily begin at temperatures >1,060°C and for melt H_2O contents slightly (~10%) less than for cotectic conditions if a closed-system, incompatible, behaviour is assumed for H_2O. This is because ~10 wt% ol must crystallize before the ol + cpx cotectic is reached (Fig. 2). Although olivine in charge 4-1 (1,050°C) is the closest to the high-Fo end of the olivine natural trend (Fig. 10), it has a Fo (86.6) lower than the maximum of phenocrysts (89.6), confirming that the most Fo-rich olivines crystallized at temperatures >1,050°C. Temperatures of a minimum of 1,100°C are implied by the most magnesian spinel phenocryst

in STV301 (Fig. 13a). For $T > 1{,}050°C$ but melt H_2O contents <4 wt%, experimental ol have CaO contents higher than the natural compositions (Fig. 10). An ol with $Fo_{88.7}$ and 0.20 wt% CaO crystallized in one additional 4 kbar STV301 experiment at 1,150°C and for 5.9 wt% H_2O in melt (Pichavant et al., in preparation). Taking a melt H_2O content of 5 wt%, a liquidus temperature of ~ 1,160°C is obtained for the parental Soufriere melts (Mg# = 73.5) by interpolating the liquidus temperatures for STV301 (Mg# = 76.8) and STV315 (Mg# = 69, calculations at NNO + 1). Although based on experimental data obtained at 4 kbar, this inferred liquidus temperature will not vary significantly with pressure because experiments on STV301 have shown that, between 8–15 kbar and for a melt H_2O content of 4.5 wt%, the slope of the ol liquidus is nearly vertical in *P–T* space (Pichavant et al. *2002a*) (Fig. 14).

The most magnesian spinel composition has a Fe^{3+}/Σ Fe ratio suggesting equilibration at $\Delta NNO = +1.5–2.0$ (Fig. 13b). These strongly oxidizing conditions are consistent with redox states inferred for the Grenada lavas (Parkinson et al. *2003*), and provide further evidence for the existence of oxidized primitive basaltic liquids.

Magmatism in the Lesser Antilles arc

One important conclusion from this paper is the demonstration that the primitive phenocryst assemblage present in Soufriere lavas crystallized from near-primary parental melts containing ~5 wt% H_2O. From an estimate of the H_2O content of the subarc mantle source, Pichavant et al. (*2002a*) suggested that high-MgO (12.5 wt%) primary melts may have H_2O concentrations as high as 5.5 wt%. Therefore, the H_2O concentration determined here for the primitive Soufriere liquids lies within the range considered possible for Lesser Antilles mantle melts. Since the Soufriere rocks are representative of the primitive group from the southern part of the arc, it is likely that lavas from Grenada, Kick'em Jenny and the Grenadines can have H_2O contents similar to those determined here for St Vincent. Parental melts with ~5 wt% H_2O will differentiate to more water-rich residual melts. For example, since 30–40% ol + cpx + sp crystallization is necessary to drive the melt from HMB to HAB composition (Fig. 6; see also Sisson and Grove *1993b*), HAB-like melts with 7–8 wt% H_2O will be generated, if water follows a closed-system, incompatible, behaviour. This range is consistent with melt H_2O concentrations calculated by applying the Al_2O_3 in melt hygrometer to the Soufriere and St. Vincent inclusions (Fig. 9), and with the presence of amphibole as a major phase in the gabbroic cumulates at St Vincent and elsewhere in the arc.

The H_2O-rich nature of the Soufriere parental liquids may seem to be inconsistent with evidence suggesting drier conditions, such as glass inclusion data and high-pressure phase equilibria. For example, Pichavant et al. (*2002a*) concluded that HMB are extracted relatively dry (~ 2 wt% H_2O) from their mantle source, and erupted/emplaced virtually unmodified at the surface. In contrast, this study shows that other HMB liquids are more water-rich. Therefore, primitive basaltic liquids at Soufriere have a range of H_2O concentrations (2–5 wt%). Only the driest may erupt unmodified while the more water-rich crystallize and differentiate at depth, producing the more fractionated members of the Soufriere suite. The variability of primary arc magmas in terms of H_2O contents may reflect temporal and spatial heterogeneities of H_2O distribution in the mantle wedge.

Conclusions

1. Primitive basaltic liquids from the Lesser Antilles arc have been experimentally crystallized at crustal pressures, under oxidizing conditions and in the presence of added water. The experiments simulate the early stages of fractionation in calc-alkaline magma series.
2. In the presence of water, crystallization of olivine and clinopyroxene is promoted, plagioclase crystallization is suppressed. Early spinel crystallization is favoured by the presence of H_2O, but also by high fO_2 and high bulk Cr. The earliest stages of fractionation of primitive arc basalts are dominated by crystallization of ol + cpx + sp assemblages. Orthopyroxene crystallization is restricted to >53 wt% SiO_2 in the coexisting melt, and is suppressed by high melt H_2O contents and oxidizing fO_2.
3. Residual melts from the crystallization of ol + cpx + sp assemblages are depleted in MgO, to a lesser extent in FeO_t, and in Ol and Cpx components. They are enriched in SiO_2, Al_2O_3, CaO, alkalis and Qz and Plag components, producing evolved compositions typical of the arc sequence. HAB are generated after 30–40% crystallization of HMB, stressing the existence of a genetic link between high-Al and high-Mg basaltic magmas in the Lesser Antilles and other arcs.
4. The role of H_2O in depressing plagioclase crystallization leads to a direct relation between the Al_2O_3 content of the residual melt and its H_2O concentration. The Al_2O_3 content of natural basaltic liquids can be used as a geohygrometer.
5. Phenocrysts in the Soufriere suite include a primitive assemblage with ol ($Fo_{89.6}$), cpx (Mg# = 90) and Cr–Al sp (Mg# = 53, Cr = 51). The presence of ol and cpx with typical mantle compositions links magma generation/equilibration in the mantle and the early crystallization history. Hornblende plays no role in the early petrogenetic evolution.
6. The most magnesian phenocrysts in the Soufriere suite crystallized from near-primary (Mg# = 73.5), hydrous (□5 wt% H_2O) and very oxidized (ΔNNO = +1.5–2.0) HMB liquids at middle crustal pressures and temperatures from ~1,160 to ~1,060°C. These liquids were parental to HAB melts containing 7–8 wt% dissolved H_2O.
7. At Soufriere, the primitive basaltic liquids have a range of H_2O concentrations (2–5 wt%). Only the driest erupt whilst the more water-rich crystallize and differentiate at depth.

Acknowledgments

Financially supported by the Natural Environment Research Council (UK) and the DYETI and ANR programs (France). We thank A.-S. Bouvier for her unpublished glass inclusion analyses. Constructive reviews and comments by O. Müntener and P. Ulmer and the editorial suggestions of T. Grove considerably improved the presentation of this study.

References

Albarède F (1995) Introduction to geochemical modelling. Cambridge University Press, Cambridge, p 543

Arculus RJ (1976) Geology and geochemistry of the alkali basalt-andesite association of Grenada, Lesser Antilles island arc. Bull Soc Geol Am 87:612–624

Arculus RJ (1978) Mineralogy and petrology of Grenada, Lesser Antilles island arc. Contrib Mineral Petrol 65:413–424

Arculus RJ (1994) Aspects of magma genesis in arcs. Lithos 33:189–208

Arculus RJ, Wills KJA (1980) The petrology of plutonic blocks and inclusions from the Lesser Antilles island arc. J Petrol 21:743–799

Baker MB, Grove TL, Price R (1994) Primitive basalts and andesites from the Mt Shasta region, N California: products of varying melt fraction and water content. Contrib Mineral Petrol 118:111–129

Ballhaus C, Berry RF, Green DH (1991) High pressure experimental calibration of the olivine-orthopyroxene-spinel oxygen geobarometer: implications for the oxidation state of the upper mantle. Contrib Mineral Petrol 107:27–40

Barclay J, Carmichael ISE (2004) A hornblende basalt from western Mexico: water-saturated phase relations constrain a pressure–temperature window of eruptibility. J Petrol 45:485–506

Barclay J, Rutherford MJ, Carroll MR (1998) Experimental phase equilibria constraints on pre-eruptive storage conditions of the Soufriere Hills magma. Geophys Res Lett 25:3437–3440

Bardintzeff JM (1983) Les verres et les magmas de l'éruption de 1979 de la Soufrière de Saint-Vincent (Antilles). Bull Soc Gèol Fr XXV(7):811–818

Bartels KS, Kinzler RJ, Grove TL (1991) High pressure phase relations of primitive high-alumina basalts from Medicine Lake volcano, northern California. Contrib Mineral Petrol 108:253–270

Brandon AD, Draper DS (1996) Constraints on the origin of the oxidation state of mantle overlying subduction zones: an example from Simcoe, Washington, USA. Geochim Cosmochim Acta 60:1739–1749

Brophy JG (1989) Can high-alumina arc basalt be derived from low-alumina arc basalt ? Evidence from Kanaga island, Aleutian arc, Alaska. Geology 17:333–336

Burnham CW (1979) The importance of volatile constituents. In: Yoder HS (ed) The Evolution of Igneous Rocks. Princeton University Press, pp 439–482

Cawthorn RG, Curran EB, Arculus RJ (1973) A petrogenetic model for the origin of the calc-alkaline suite of Grenada, Lesser Antilles. J Petrol 14:327–337

Costa F, Scaillet B, Pichavant M (2004) Petrological and experimental constraints on the pre-eruption conditions of Holocene dacite from Volcán San Pedro (36°S, Chilean Andes) and the importance of sulphur in silicic subduction-related magmas. J Petrol 45:855–881

Crawford AJ, Falloon TJ, Eggins S (1987) The origin of island arc high-alumina basalts. Contrib Mineral Petrol 97:417–430

Devine JD, Sigurdsson H (1983) The liquid composition and crystallization history of the 1979 Soufriere magma, St Vincent, WI. J Volcanol Geotherm Res 16:1–31

Devine JD, Sigurdsson H (1995) Petrology and eruption styles of Kick'em-Jenny submarine volcano, Lesser Antilles island arc. J Volcanol Geotherm Res 69:35–58

Devine, JD, Gardner JE, Brack HP, Layne GD, Rutherford MJ (1995) Comparison of microanalytical methods for estimating H_2 *O* contents of silicic volcanic glasses. Am Mineral 80:319–328

Di Carlo I, Pichavant M, Rotolo S, Scaillet B (2006) Experimental crystallization of a high-*K* arc basalt: the golden pumice, Stromboli volcano (Italy). J Petrol 47:1317–1343

Draper DS, Johnston AD (1992) Anhydrous PT phase relations of an Aleutian high-MgO basalt: an investigation of the role of olivine-liquid reaction in the generation of arc high-alumina basalts. Contrib Mineral Petrol 112:501–519

Eggins SM (1993) Origin and differentiation of picritic arc magmas, Ambae (Aoba), Vanuatu. Contrib Mineral Petrol 114:79–100

Gaetani GA, Grove TL (1998) The influence of water on the melting of mantle peridotite. Contrib Mineral Petrol 131:323–346

Gaetani GA, Grove TL, Bryan WB (1993) The influence of water on the petrogenesis of subduction-related igneous rocks. Nature 365:332–334

Gaetani GA, Grove TL, Bryan WB (1994) 32. Experimental phase relations of basaltic andesite from hole 839B under hydrous and anhydrous conditions. Proceedings of the Ocean Drilling Program, Scientific Results 135:557–563

Gill JB (1981) Orogenic andesites and plate tectonics. Springer, Heidelberg

Graham AM (1981) Melting relations of island arc lavas from Grenada, Lesser Antilles. In: Ford CE (ed) Progress in experimental petrology, NERC Publications Series D, pp 126–132

Graham AM, Thirlwall MF (1981) Petrology of the 1979 eruption of Soufriere volcano, St Vincent, Lesser Antilles. Contrib Mineral Petrol 76:336–342

Grove TL, Baker MB (1984) Phase equilibrium controls on tholeiitic versus calc-alkaline differentiation trends. J Geophys Res 89:3252–3274

Grove TL, Elkins-Tanton LT, Parman SW, Chatterjee N, Müntener O, Gaetani GA (2003) Fractional crystallization and mantle-melting controls on calc-alkaline differentiation trends. Contrib Mineral Petrol 145:515–533

Gust DA, Perfit MR (1987) Phase relations of a high-Mg basalt from the Aleutian Island Arc: Implications for primary island arc basalts and high-Al basalts. Contrib Mineral Petrol 97:7–18

Heath E, Macdonald R, Belkin HE, Hawkesworth CJ, Sigurdsson H (1998) Magmagenesis at Soufriere volcano, St Vincent, Lesser Antilles arc. J Petrol 39:1721–1764

Holloway JR (1987) Igneous fluids. In: Eugster HP, Carmichael ISE (eds) Thermodynamic modelling of geological materials: minerals, fluids and melts. Mineralogical Society of America, Reviews in Mineralogy 17, pp 211–233

Holloway JR, Burnham CW (1972) Melting relations of basalt with equilibrium water pressure less than total pressure. J Petrol 13:1–29

Kress V, Carmichael ISE (1991) The compressibility of silicate liquids containing Fe2O3 and the effect of composition, temperature, oxygen fugacity and pressure on their redox states. Contrib Mineral Petrol 108 82:92

Lesne P (2004) Les conditions pré-éruptives d'un liquide basique de la Soufrière, Guadeloupe. DEA, University of Orléans, p 46

Lewis JF (1973a) Petrology of the ejected plutonic blocks of the Soufriere volcano, St Vincent, West Indies. J Petrol 14:81–112

Lewis JF (1973b) Mineralogy of the ejected plutonic blocks of the Soufriere volcano, St Vincent: olivine, pyroxene, amphibole and magnetite paragenesis. Contrib Mineral Petrol 38:197–220

Lindsley DH (1983) Pyroxene thermometry. Am Mineral 68:477–493

Macdonald R, Hawkesworth CJ, Heath E (2000) The Lesser Antilles volcanic chain: a study in arc magmatism. Earth Sci Rev 49:1–76

Marcelot G, Le Guen de Kerneizon M, Bohn M (1981) Zonation du nickel et du chrome dans les minéraux ferromagnésiens d'un basalte de Saint-Vincent (Petites Antilles); conséquences pétrogénétiques. CR Acad Sci Paris 293:1079–1081

Martel C, Pichavant M, Bourdier J-L, Traineau H, Holtz F, Scaillet B (1998) Magma storage conditions and control of eruption regime in silicic volcanoes: experimental evidence from Mt. Pelée. Earth Planet Sci Lett 156:89–99

Martel C, Pichavant M, Holtz F, Scaillet B, Bourdier J-L, Traineau H (1999) Effects of fO_2 and H_2O on andesite phase relations between 2 and 4 kbar. J Geophys Res 104:29453–29470

Miyashiro A (1974) Volcanic rock series in island arcs and active continental margins. Am J Sci 275:321–355

Müntener O, Kelemen P, Grove TL (2001) The role of H_2O during crystallization of primitive arc magmas under uppermost mantle conditions and genesis of igneous pyroxenites: an experimental study. Contrib Mineral Petrol 141:643–658

Nye CJ, Reid MR (1986) Geochemistry of primary and least fractionated lavas from Okmok volcano, central Aleutians: implications for arc magmagenesis. J Geophys Res 91:10271–10287

Parkinson IJ, Arculus RJ, Eggins SM (2003) Peridotite xenoliths from Grenada, Lesser Antilles island arc. Contrib Mineral Petrol 146:241–262

Pichavant M, Macdonald R (2003) Mantle genesis and crustal evolution of primitive calc-alkaline basaltic magmas from the Lesser Antilles arc. In: Larter RD, Leat PT (eds) Intra-oceanic subduction systems: tectonic and magmatic processes. Special Publications 219, The Geological Society, London, pp 239–254

Pichavant M, Mysen BO, Macdonald R (2002a) Source and H_2O content of high-MgO magmas in island arc settings: an experimental study of a primitive calc-alkaline basalt from St. Vincent, Lesser Antilles arc. Geochim Cosmochim Acta 66:2193–2209

Pichavant M, Martel C, Bourdier J-L, Scaillet B (2002b) Physical conditions, structure and dynamics of a zoned magma chamber: Mount Pelée (Martinique, Lesser Antilles arc). J Geophys Res 107:ECV 2 1–ECV30. doi:10.1029/2001JB000315

Poussineau S (2005) Dynamique des magmas andésitiques: approche expérimentale et pétrostructurale; application à la Soufrière de Guadeloupe et à la Montagne Pelée. PhD thesis, University of Orléans, p 295

Pownceby MI, O'Neill HStC (1994) Thermodynamic data from redox reactions at high temperatures. III. Activity-composition relations in Ni–Pd alloys from EMF measurements at 850–1250 K and calibration of the NiO + Ni–Pd assemblage as a redox sensor. Contrib Mineral Petrol 116:327–339

Prouteau G, Scaillet B (2003) Experimental constraints on the origin of the 1991 Pinatubo dacite. J Petrol 44:2203–2241

Robie RA, Hemingway BS, Fisher JR (1979) Thermodynamic properties of minerals and related substances at 298.15 K and 1 bar (10^5 pascals) pressure and at higher temperatures. US Geol Surv Bull 1452

Roggensack K (2001) Unraveling the 1974 eruption of Fuego volcano (Guatemala) with small crystals and their young melt inclusions. Geology 29:911–914

Roggensack K, Hervig RL, McKnight SB, Williams SN (1997) Explosive basaltic volcanism from Cerro Negro volcano: influence of volatiles on eruptive style. Science 277:1639–1642

Rohrbach A, Schuth S, Ballhaus C, Münker C, Matveev S, Qopoto C (2005) Petrological constraints on the origin of arc picrites, New Georgia group, Solomon islands. Contrib

Mineral Petrol 149:685–698

Roux J, Lefèvre A (1992) A fast quench device for IHPV. Eur J Mineral 4:279–281

Roux J, Holtz F, Lefèvre A, Schulze F (1994) A reliable high temperature setup for internally heated pressure vessel: applications to silicate melt studies. Am Mineral 79:1145–1149

Rutherford MJ, Devine JD (2003) Magmatic conditions and magma ascent as indicated by hornblende phase equilibria and reactions in the 1995–2002 Soufriere Hills magma. J Petrol 44:1433–1454

Scaillet B, Evans BW (1999) The June 15 1991 eruption of Mount Pinatubo. 1. Phase equilibria and pre-eruption P-T-fO2-fH2O conditions of the dacite magma. J Petrol 40:381–411

Scaillet B, Pichavant M, Roux J, Humbert G, Lefèvre A (1992) Improvements of the Shaw membrane technique for measurement and control of *f*H2 at high temperatures and pressure. Am Mineral 77:647–655

Scaillet B, Pichavant M, Roux J (1995) Experimental crystallization of leucogranite magmas. J Petrol 36:663–705

Schiano P, Clocchiatti R, Boivin P, Médard E (2004) The nature of melt inclusions inside minerals in an ultramafic cumulate from Adak volcanic enter, Aleutian arc: implications for the origin of high-alumina basalts. Chem Geol 203:169–179

Sisson TW, Grove TL (1993a) Experimental investigations of the role of H_2O in calc-alkaline differentiation and subduction zone magmatism. Contrib Mineral Petrol 113:143–166

Sisson TW, Grove TL (1993b) Temperatures and H_2O contents of low-MgO high alumina basalts. Contrib Mineral Petrol 113:167–184

Smith TE, Thirlwall MF, MacPherson C (1996) Trace-element and isotope geochemistry of the volcanic rocks of Bequia, Grenadine islands, Lesser Antilles arc: a study of subduction enrichment processes. J Petrol 37:117–143

Tatsumi Y, Sakuyama M, Fukuyama H, Kushiro I (1983) Generation of arc basalt magmas and thermal structure of the mantle wedge in subduction zones. J Geophys Res 88:5815–5825

Taylor JR, Wall VJ, Pownceby MI (1992) The calibration and application of accurate redox sensors. Am Mineral 77:284–295

Tormey DR, Grove TL, Bryan WB (1987) Experimental petrology of normal MORB near the Kane fracture zone: 22°–25°N, mid-Atlantic ridge. Contrib Mineral Petrol 96:121–139

Ulmer P (1989) The dependence of the Fe^{2+} - Mg cation-partitioning between olivine and basaltic liquid on pressure, temperature and composition. Contrib Mineral Petrol 101:261–273

Westercamp D (1988) Magma generation in the Lesser Antilles: geological constraints. Tectonophys 149:145–163

Westercamp D, Mervoyer B (1976) Les séries volcaniques de la Martinique. Bull BRGM 2-IV:231–242

Yoder HS Jr (1965) Diopside-anorthite-water at five and ten kilobars and its bearing on explosive volcanism. Yearb Carnegie Inst Wash 64:82–89

Zellmer GF, Hawkesworth CJ, Sparks RSJ, Thomas LE, Harford CL, Brewer TS, Loughlin SC (2003) Geochemical evolution of the Soufriere Hills volcano, Lesser Antilles volcanic arc. J Petrol 44:1349–1374

Figures

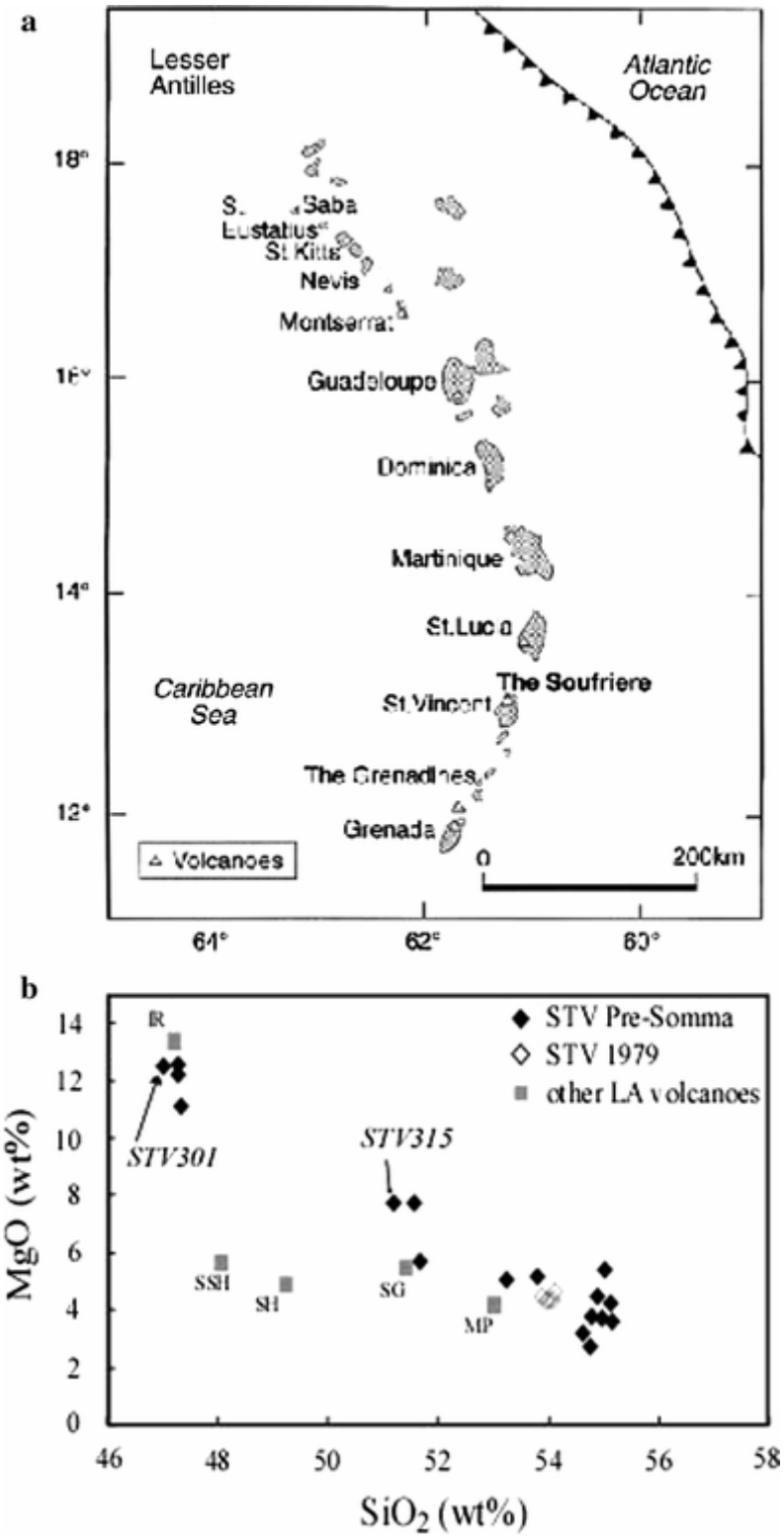

Fig. 1 **a** Map of the Lesser Antilles arc showing the main islands and active volcanoes, after Heath et al. (*1998*). **b** Variation diagram showing compositions of selected mafic lavas from St Vincent and other volcanoes from the arc. *STV* Soufriere, St Vincent (Pre-Somma lavas: Heath et al. *1998*; 1979 lavas: Graham and Thirlwall *1981*); *IR* Ilet à Ramiers, Martinique (Westercamp and Mervoyer *1976*); *SSH* and *SH*, respectively, South Soufriere Hills and Soufriere Hills, Montserrat (Zellmer et al. *2003*); *S*

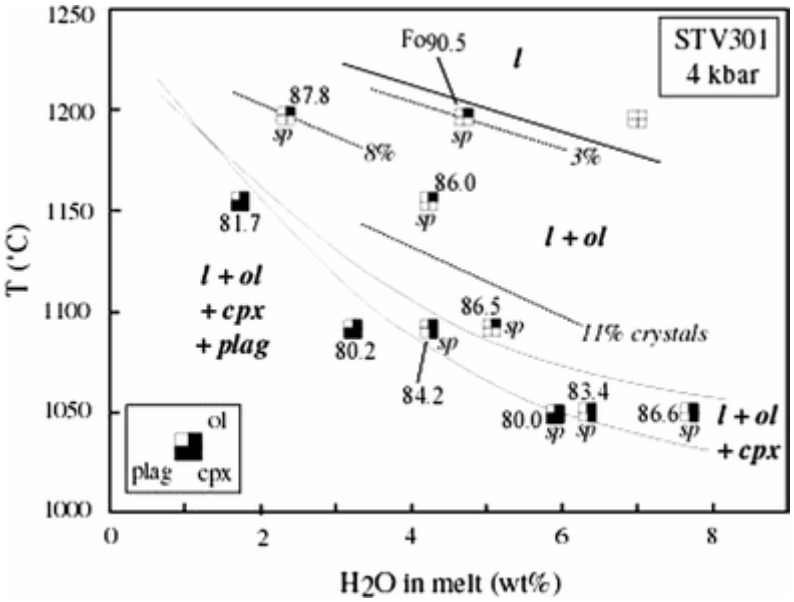

Fig. 2 Near-liquidus 4 kbar T-H_2O in melt phase diagram for high-MgO basalt STV301 showing experimental data points, saturation curves and stability fields. *l* liquid (silicate melt); *ol* olivine; *cpx* clinopyroxene; *plag* plagioclase; *sp* Cr–Al spinel. Presence of spinel indicated by sp adjacent to the data points. The proportion (3, 8, 11 wt%) of crystals present in the l + ol field is contoured. Data points are labelled with the Fo content of olivine. All data in Tables 3 and 4

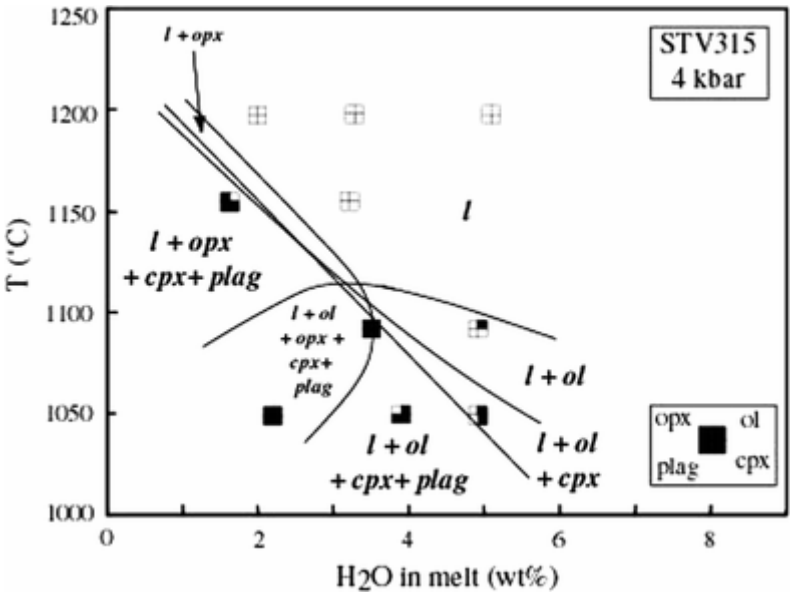

Fig. 3 Near-liquidus 4 kbar T-H_2O in melt phase diagram for basalt STV315 showing experimental data points, saturation curves and stability fields. *Opx* orthopyroxene, other abbreviations as in Fig. 2. All data in Table 3

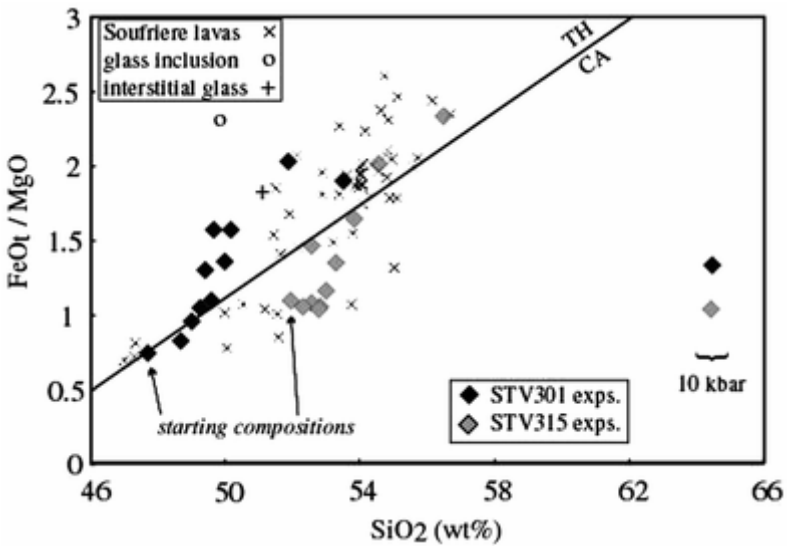

Fig. 4 Plot of FeO_t/MgO versus SiO_2 (Miyashiro *1974*) for experimental glasses (this study) and Soufriere natural products. Lava whole-rock compositions from Graham and Thirlwall (*1981*) and Heath et al. (*1998*). Glass inclusion represents the average of melt inclusions in olivine from the 1979 eruption (Devine and Sigurdsson *1983*). Interstitial glass represents the composition of an interstitial scoria from a gabbroic cumulate (Lewis *1973a*). Experimental data at 4 kbar except otherwise stated (10 kbar)

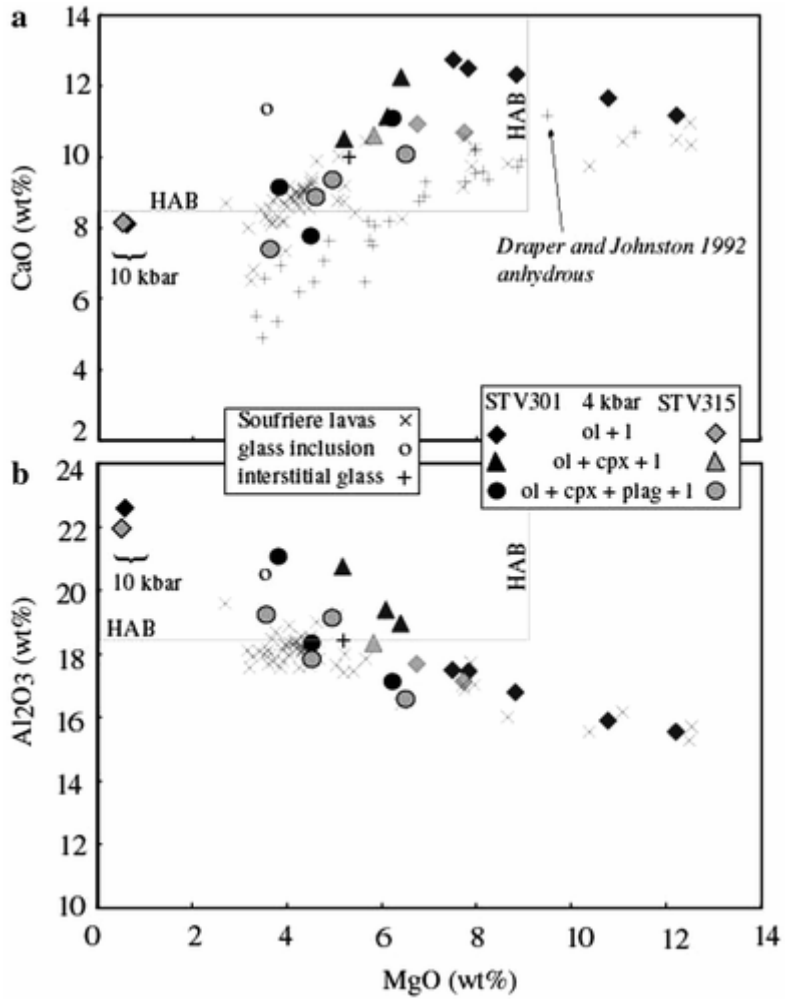

Fig. 5 MgO variation diagrams (**a** CaO; **b** Al_2O_3) for experimental glasses (this study) and Soufriere natural products (Fig. 4). Experimental data at 4 kbar except otherwise stated (10 kbar). Data points separated by phase assemblage, with starting glasses and ol + l charges plotted under the same symbol. For STV315, all cpx + plag-

bearing charges, either ol-bearing, ol-free or opx-bearing are plotted under the same symbol. In (**a**), the experimental glasses from the anhydrous high-pressure experiments of Draper and Johnston (*1992*) are shown for comparison with the hydrous trends from this study. The HAB (high-alumina basalt) *boxes* are constructed from the compositional criteria suggested by Draper and Johnston (*1992*). Abbreviations as in Fig. 2

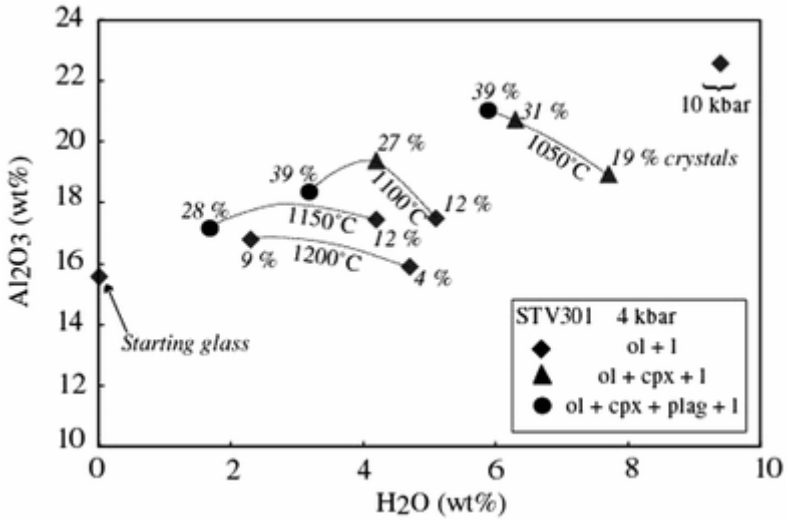

Fig. 6 Al_2O_3 contents of experimental liquids as a function of their melt H_2O content. Experimental data for STV301 only and at 4 kbar except otherwise stated (10 kbar). Data points separated by phase assemblage, as in Fig. 5, and labelled with proportions of crystals in the charges (wt%, Table 3). Abbreviations as in Fig. 2

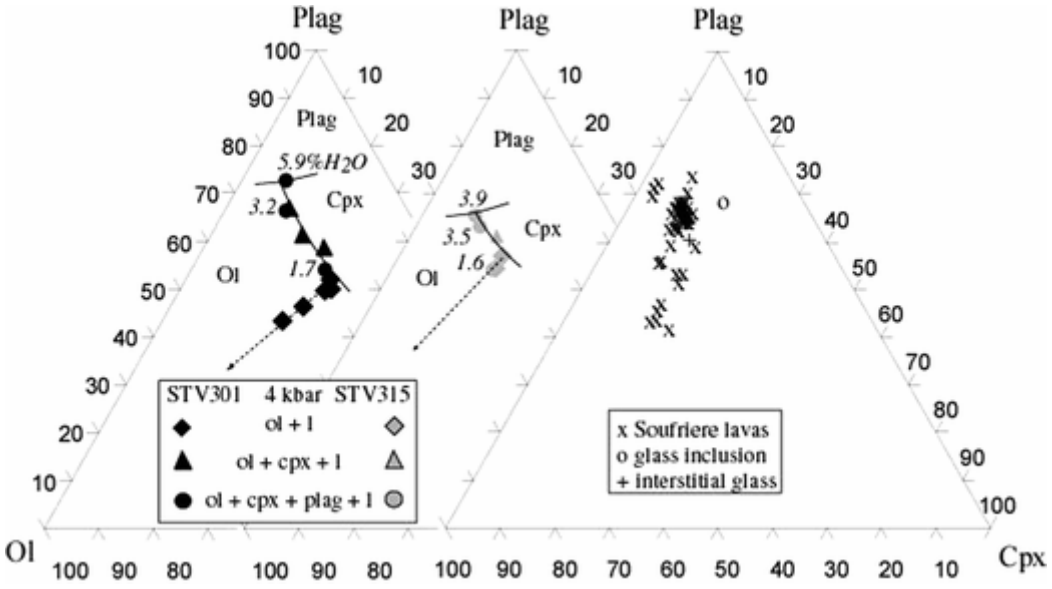

Fig. 7 Pseudo-ternary Ol-Plag-Cpx diagrams showing compositions of experimental glasses (STV301: left diagram; STV315: middle diagram) and Soufriere natural products (right diagram, significance of data points as in Fig. 4). Projection scheme of Tormey et al (*1987*). Data points separated by phase assemblage, as in Fig. 5. Ol + cpx + plag + l data points labelled with melt H_2O concentrations (see text). Stability field and field boundaries (*curved lines*) are indicated. *Dashed lines* are olivine control lines. Corundum-normative glasses 1–5, 1–9 (10 kbar charges) and glass 4–6 (see text) are not shown. For clarity, the supraliquidus glasses 6-4, 7-4, 7-5, 7-6 (STV315) have not been plotted. Abbreviations as in Fig. 2

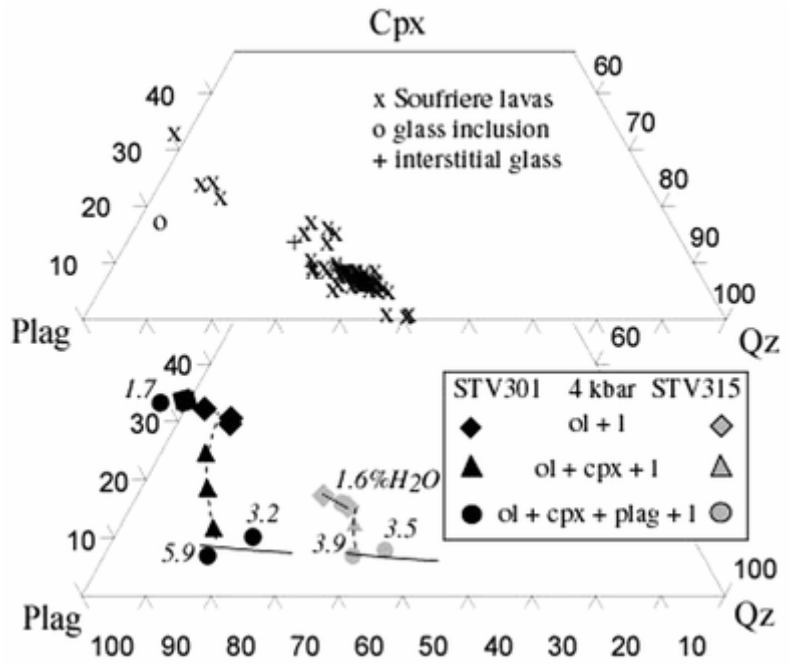

Fig. 8 Pseudo-ternary Plag-Cpx-Qz diagrams showing compositions of experimental glasses (*lower diagram*) and Soufriere natural products (*upper diagram*, significance of data points as in Fig. 4). Projection scheme of Tormey et al. (*1987*). Data points separated by phase assemblage, as in Fig. 5. Ol + cpx + plag + l data points labelled with melt H_2O concentrations (see text). Liquid paths for ol (*dotted*), ol + cpx (*dashed*) and ol + cpx + plag +/- opx (*solid lines*) fractionating assemblages are outlined. Corundum-normative glasses 1-5, 1-9 (10 kbar charges) and glass 4-6 (see text) are not shown. For clarity, the supraliquidus glasses 6-4, 7-4, 7-5, 7-6 (STV315) have not been plotted. Abbreviations as in Fig. 2

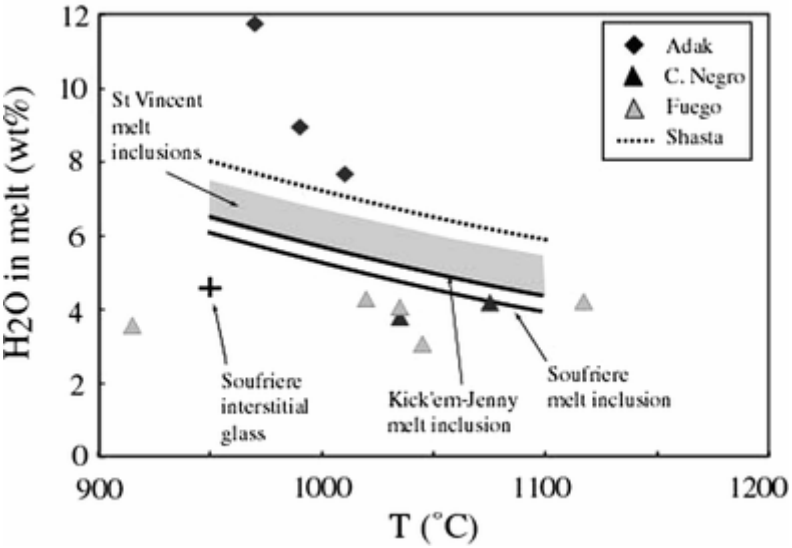

Fig. 9 Calculated melt H_2O contents and temperatures for selected arc basaltic liquids. The calculations use the geohygrometer described in text and Table 5. Input data for the calculations are major element compositions of melt inclusion except for one interstitial glass from a Soufriere gabbroic cumulate. When no constraints are available on temperature, melt H_2O concentrations are calculated between 950 and 1,100°C (*solid* and *dashed curves*, *grey field*). For the interstitial glass, a temperature of 950°C is assumed. In other cases, the geohygrometer computes either H_2O in melt when temperature is available (Adak) or temperature when the melt H_2O content is known (Cerro Negro, Fuego). Compositions of the Soufriere interstitial glass from Lewis (*1973a*) and of the Soufriere inclusion from Devine and Sigurdsson (*1983*). Compositions of other melt inclusions: St Vincent (Bouvier et al. written communication, 2006), Kick'em-Jenny (Devine and Sigurdsson *1995*), Adak

(Schiano et al. *2004*), Cerro Negro (Roggensack et al. *1997*), Fuego (Roggensack *2001*), Shasta (Sisson and Grove *1993b*)

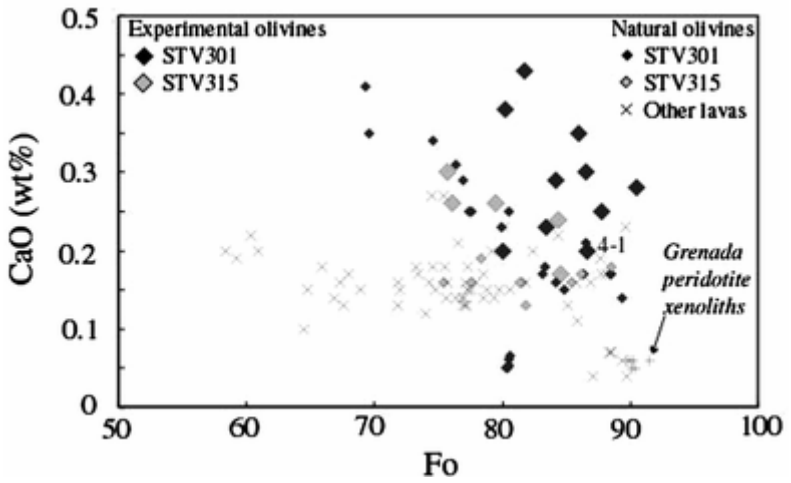

Fig. 10 CaO in experimental (this study) and natural (Marcelot et al. *1981*; Heath et al. *1998*) olivines plotted as a function of their forsterite (Fo) content. Compositions of olivines in peridotite xenoliths from Grenada after Parkinson et al. (*2003*). Olivine composition in charge 4-1 (discussed in text) is indicated

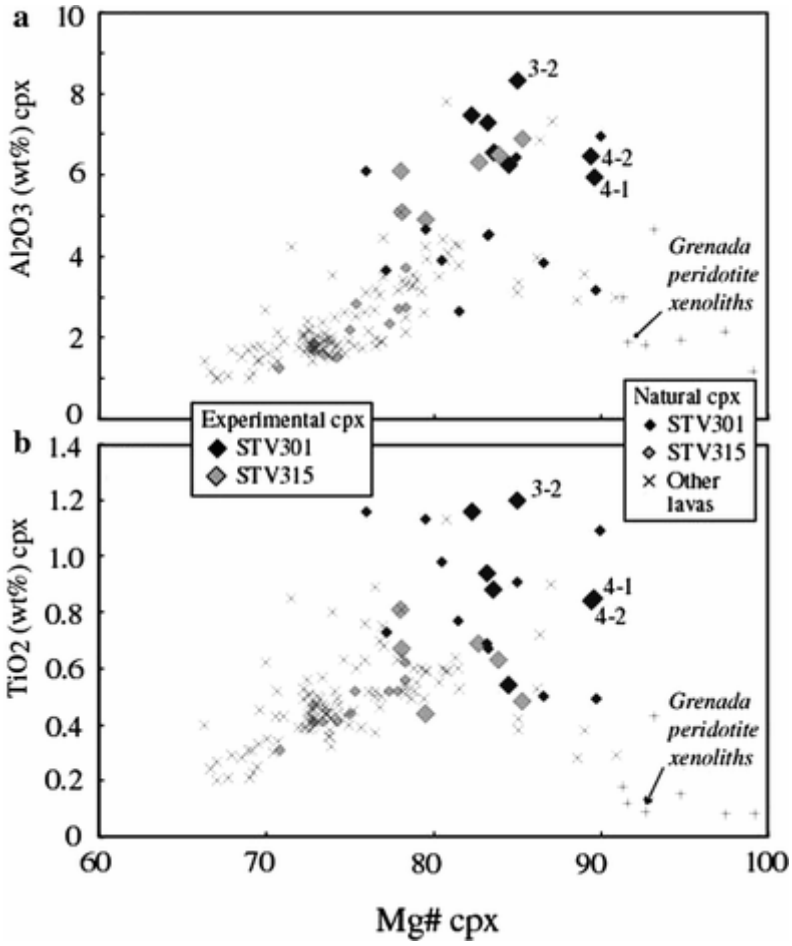

Fig. 11 Al_2O_3 (**a**) and TiO_2 (**b**) in experimental (this study) and natural (Graham and Thirlwall *1981*; Marcelot et al. *1981*; Heath et al. *1998*) clinopyroxenes plotted as a function of their Mg#, calculated with $Fe = Fe^{2+}$. Compositions of cpx in peridotite xenoliths from Grenada after Parkinson et al. (*2003*). Cpx compositions in charges 4-1, 4-2 and 3-2 (discussed in text) are indicated

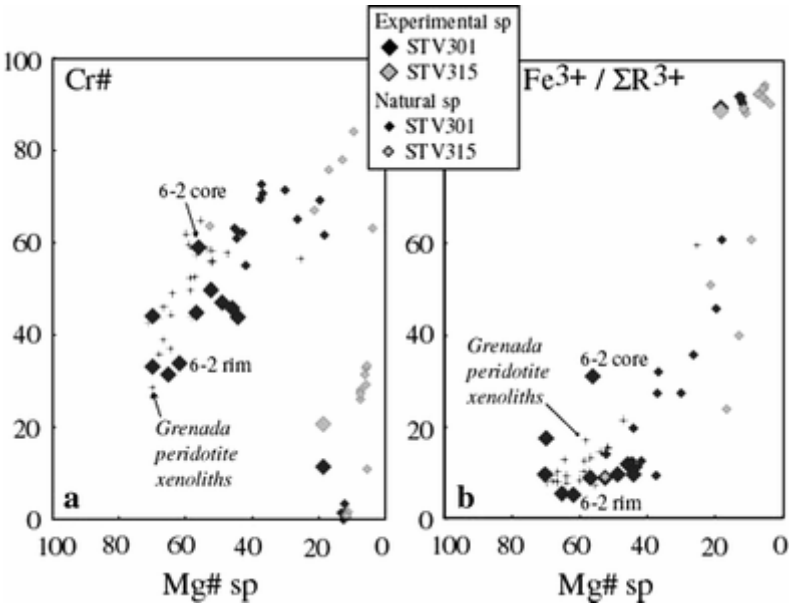

Fig. 12 Cr# (**a**) and $Fe^{3+}/\Sigma R^{3+}$ (**b**) in experimental (this study) and natural (Marcelot et al. *1981*; Heath et al. *1998*) spinels as a function of their Mg#. Cr–Al spinels and magnetite plotted with the same symbol. Compositions of spinel in peridotite xenoliths from Grenada after Parkinson et al. (*2003*). Core and rim indicate compositions of the partially reacted spinel grain in charge 6-2 (see text). For charges 4-1, 4-2, 4-3, 3-1, 3-2, the corrected spinel compositions are plotted (see text)

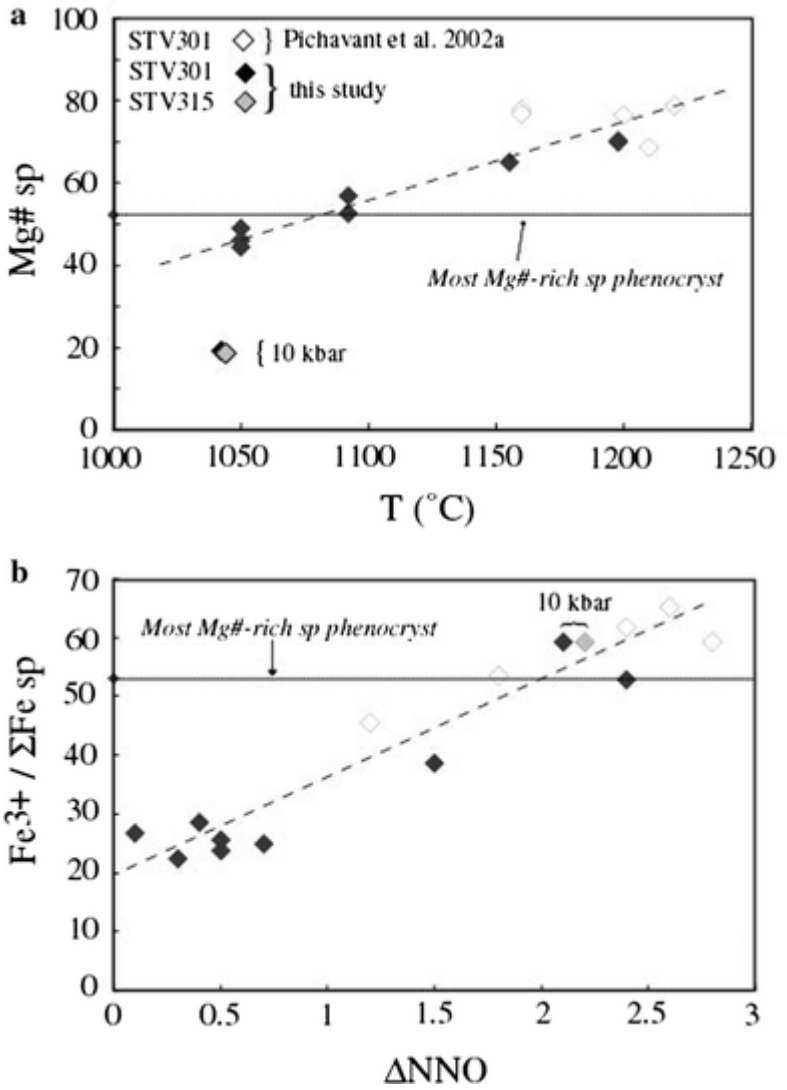

Fig. 13 Compositions of experimental spinels. (**a**) Mg# vs. temperature; (**b**) Fe^{3+}/Σ Fe versus ΔNNO. Cr–Al spinels and magnetite plotted with the same symbol. Data from this study (*black* and *grey symbols*) at 4 kbar except otherwise stated (10 kbar), and from Pichavant et al. (*2002a*) at 10–15 kbar (*open symbols*). The horizontal lines drawn give the Mg# (**a**) and the Fe^{3+}/Σ Fe (**b**) of the most Mg#-rich sp of the Soufriere suite, respectively (see Fig. 12). *Dashed lines* are hand-drawn regressions of the experimental data points. In **a**, the two 10 kbar magnetites have lower Mg# than the regression line since they coexist with high amounts of Mg-rich hornblende (Table 3). Corrected spinel compositions plotted for experiments < 1,100°C (see text)

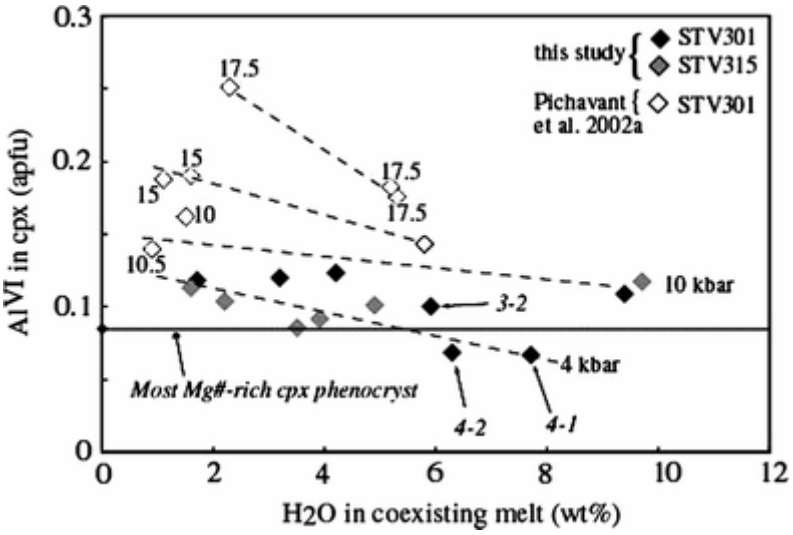

Fig. 14 Al^{VI} in experimental clinopyroxenes (atom per formula unit, apfu) plotted as a function of the H_2O content of the coexisting melt (wt%) for STV301 at different pressures and STV315 at 4 kbar. Experimental data at 4 and 10 kbar (*black* and *grey symbols*) from this study; Experimental data at 10–17.5 kbar (*open symbols*) from Pichavant et al. (*2002a*) with data points labelled with pressure in kbar. The horizontal line drawn gives the Al^{VI} of the most Mg#-rich cpx of the Soufriere suite (see Fig. 11). Dashed lines are hand-drawn regressions of the experimental data points. 4-1, 4-2, 3-2 refer to experimental charges (Table 3)

Tables

Table 1 Major element compositions

Sample	STV301		STV315		PAR1	PAR2
	Whole-rock[a]	Glass[b]	Whole-rock[a]	Glass[c]		
SiO_2 (wt%)	47.01	46.9(4)	51.20	51.3(3)	48.05	48.44
TiO_2	1.07	1.08(3)	0.82	0.77(8)	1.17	1.15
Al_2O_3	15.28	15.3(2)	16.88	16.9(1)	16.51	17.01
FeO_t	8.79	8.96(17)[d]	8.06	8.43(31)	9.07	8.65
MnO	0.16	0.17(3)	0.16	0.16(9)	0.16	0.13
MgO	12.50	12.0(1)	7.76	7.64(11)	9.90	10.55
CaO	10.96	11.0(1)	10.55	10.6(2)	11.88	10.99
Na_2O	2.23	2.27(7)	2.33	2.59(12)	2.45	2.33
K_2O	0.47	0.49(2)	0.33	0.34(5)	0.52	0.53
H_2O	ND	0.10[e]	ND	ND	0	0
Total	98.47	98.27	98.09	98.73	99.71	99.78
Cr (ppm)	728	680	303	140		
Ni	250	ND	75	ND		
CIPW norm						
q	–		1.29		–	–
or	2.78		1.95		3.07	3.13
ab	18.48		15.54		14.04	14.99
an	29.64		38.80		37.59	39.11
ne	0.56		–		0.88	–
di	19.32		14.37		21.34	16.21
hy	–		22.77		–	4.29
ol	23.67		–		18.53	17.92
mt	2.13		1.94		2.19	2.09
il	2.03		1.56		2.22	2.18
Vol% phenocrysts						
Olivine	22.0		11.2			
Spinel	4.3		3.0			
Clinopyroxene	6.2		5.1			
Plagioclase	–		45.9			
Orthopyroxene	–		Trace			

[a]XRF spectrometry (Heath et al. *1998*)
[b]Average of 41 electron microprobe analyses (Pichavant et al. *2002a*); numbers in brackets are standard deviations in terms of least unit cited
[c]Average of 10 electron microprobe analyses
[d]FeO = 1.52 wt% and Fe_2O_3 = 8.26 wt%; Fe^{3+}/Fe^{2+} (at.) determined by Mössbauer spectroscopy (Pichavant et al. *2002a*)
[e]H_2O by Karl-Fischer titration
For all CIPW calculations, at. Fe^{3+}/total Fe = 0.15. PAR1 and PAR2 are calculated compositions of liquids parental to the Soufriere suite (see text)

Table 2 Representative electron microprobe analyses of phenocrysts

Sample	Phase	SiO_2	TiO_2	Al_2O_3	Cr_2O_3	FeO_t	MnO	MgO	CaO	Na_2O	K_2O	NiO	Total	Mg#	mol%
STV301	Ol (c)	40.8	0.02	0.03	0.03	11.4	0.19	48.5	0.17	0.01	NA	0.22	101.4	88.3	$Fo_{88.3}$
	Ol (r)	38.9	0.02	0.01	0.01	20.9	0.48	40.2	0.25	0	NA	0.09	100.9	77.4	$Fo_{77.4}$
	Cpx	48.6	0.91	6.42	0.69	5.43	0.09	14.2	22.2	0.23	NA	0.02	98.9	85.0	$En_{43}Wo_{49}$
	Sp	0.09	0.49	17.6	43.0	29.6	0.45	8.97	0.10	NA	NA	0.08	100.5	42.8	$Cr\#_{62}$
STV315	Ol (c)	40.8	0.03	0.02	0.04	11.3	0.22	48.7	0.18	0.01	NA	0.17	101.5	88.4	$Fo_{88.4}$
	Ol (r)	39.3	0.04	0.02	0.04	20.1	0.36	40.7	0.19	0.01	NA	0.09	100.9	78.3	$Fo_{78.3}$
	Cpx	51.8	0.44	2.19	0.03	9.97	0.41	15.29	19.32	0.27	NA	0.04	99.7	75.0	$En_{45}Wo_{41}$
	Plag	44.9	NA	35.9	NA	0.45	na	0.05	18.61	0.73	0.00	NA	100.6	19.0	An_{93}
	Opx	53.6	0.23	0.96	0.02	19.4	0.76	24.5	1.63	0.04	NA	0.02	101.2	70.4	$En_{68}Wo_3$
	Sp	0.03	4.27	6.77	20.5	59.2	0.42	4.41	0.00	NA	NA	0.10	95.7	21.3	$Cr\#_{67}$

Ol olivine, *Plag* plagioclase, *Opx* orthopyroxene, *Cpx clinopyroxene*, Sp, Cr–Al spinel; *c* core, *r* rim, *NA* not analyzed Mg# = 100* at. $Mg/(Mg + Fe^{2+})$, Fo = 100*at. Mg/(Mg + Fe) in olivine, Cr# = 100*at; Cr/(Cr + Al) in spinel, En = 100*at. $Mg/(Mg+Fe^{2+}+Ca)$, Wo = 100*at. $Ca/(Mg + Fe^{2+}+Ca)$ in pyroxene, An = 100*at. Ca/(Ca + Na + K), Or = 100*at. K/(Ca + Na + K) in plagioclase

Table 3 Experimental conditions and results

Charge	H_2O melt wt%	aH_2O	$logfO_2$ bar	ΔNNO bar	Phase assemblage[a]	ΣR^2	Fe loss[b]%	Kd^{Fe-Mg}Ol-l	Kd^{Fe-Mg}Cpx–l	Kd^{Fe-Mg}Opx–l	Kd^{Na-Ca} Plag-l
Run 4, 4,002 bars, 1,050°C, fH_2 = 12.6 bars, 23 h, XNi = 0.46, Au capsules											
STV301											
4-1	7.7[e]	0.91	−8.8	+0.7	Gl(81), Ol(12), Cpx(6), Sp(1), qu	0.07	−1	0.28	0.21		
4-2	6.3[e]	0.66	−9.1	+0.5	Gl(69), Ol(12), Cpx(18), Sp(1), qu	0.07	+1	0.29	0.17		
4-3	5.9[e]	0.60	−9.2	+0.4	Gl(51), Ol(15), Cpx,(23) Plag(10)	0.05	0	0.28	0.22		4.49
					Sp(1), qu						
STV315											
4-4	4.9[e]	0.57	−9.2	+0.3	Gl(92), Ol(4), Cpx(4), qu	0.40	−6	0.30	0.35		
4-5	3.9[e]	0.40	−9.5	+0.0	Gl(78), Ol(5), Cpx(13), Plag(4), qu	0.11	−3	0.34	0.25		3.19
4-6	2.2[e]	0.18	−10.2	−0.7	Gl(64), Ol(12), Cpx(22), Opx(−10)	0.11	+1	0.28	0.25	0.26	3.14
					Plag(12), qu						
Run 3, 4,015 bars, 1,092°C, fH_2 = 13.2 bars, 22.5 h, XNi = 0.45, AgPd capsules											
STV301											
3-1	5.1[e]	0.63	−8.5	+0.5	Gl(88), Ol(11), Sp(1), qu	0.07	+1	0.33			
3-2	4.2[e]	0.44	−8.8	+0.1	Gl(73), Ol(12), Cpx(14), Sp(1), qu	0.06	+1	0.31	0.29		
3-3	3.2[e]	0.30	−9.2	−0.2	Gl(39), Ol(18), Cpx(21), Plag(22)	1.02	−10	ND	ND		ND
					qu						

Charge	H_2O melt wt%	aH_2O	$logfO_2$ bar	ΔNNO bar	Phase assemblage[a]	ΣR^2	Fe loss[b]%	Kd^{Fe-Mg}Ol-l	Kd^{Fe-Mg}Cpx–l	Kd^{Fe-Mg}Opx–l	Kd^{Na-Ca} Plag-l
STV315											
3-5	4.9[e]	0.59	−8.6	+0.4	Gl(97), Ol(3)	0.44	−7		0.36		
3-6	3.5[e]	0.39	−8.9	+0.0	Gl(62), Ol(7), Cpx(13), Plag(18)	0.08	0	0.35	0.30	0.29	1.62
					Opx(tr), qu						
Run 6, 4,147 bars, 1155°C, fH_2 = 14.0 bars, 13 h, XNi = 0.43, AgPd capsules											
STV301											
6-1	4.2[d]	0.49	−7.9	+0.3	Gl(88), Ol(11), Sp(1), qu	0.08	−3		0.35		
6-2	1.7[e]	0.14	−9.0	−0.8	Gl(54), Ol(16), Cpx(12), Plag(18)	0.05	−2	0.29	0.27		1.28
STV315											
6-4	3.2[e]	0.36	−8.1	+0.0	Gl(100)	0.27	−4				
6-5	1.6[e]	0.14	−9.0	−0.8	Gl(73), Opx(5), Cpx(8), Plag(14)	0.20	−3		0.36	0.31	1.36
Run 7, 4,204 bars, 1,198°C, fH_2 = 1.7 bars, 25 h, XNi = 0.12, AgPd capsules											
STV301											
7-2	4.7[d]	0.63	−5.3	+2.4	Gl(96), Ol(3), Sp(1), qu	0.02	+1		0.37		
7-3	2.3[d]	0.23	−6.1	+1.5	Gl(91), Ol(8), Sp(1), qu	0.05	−2		0.37		
STV315											
7-4	5.1[f]	0.65	−5.2	+2.4	Gl(100), qu	0.80	−4				
7-5	3.3[e]	0.37	−5.7	+2.0	Gl(100)	0.43	−4				
7-6	2.0[e]	0.18	−6.4	+1.3	Gl(100)	1.04	−7				
Run 1, 9,577 bars, 1,044°C, fH_2 = 6.0 bars, 17 h, XNi = 0.15											
STV301											
1-9(Pt)	9.4[e]	0.59	−7.4	+2.1	Gl(29), Amph(64), Cpx(2),	0.28	0[b]				0.35

Charge	H_2O melt wt%	aH_2O	$logfO_2$ bar	ΔNNO bar	Phase assemblage[a]	ΣR^2	Fe loss[b]%	Kd^{Fe-Mg}Ol-l	Kd^{Fe-Mg}Cpx–l	Kd^{Fe-Mg}Opx–l	Kd^{Na-Ca} Plag-l
					Mt(5)						
STV315											
1-5(AgPd)	9.7[e]	0.62	−7.4	+2.2	Gl(52), Amph(33), Cpx(8), Mt(7)	0.68	0[b]				0.44

H_2O calculated from H_2O melt using the model of Burnham (*1979*); XNi = mole fraction of Ni in the alloy phase of the sensor; log fO_2 calculated from experimental fH_2 and fH_2O (determined from aH_2O); ΔNNO = log fO_2 − log fO_2 of the NNO buffer calculated at *P* and *T* (Pownceby and O'Neill, *1994*); *ND* not determined, tr: a trace of (phase proportion < 1% by weight)

[a] Phase proportions calculated by mass balance; *Gl* glass, *Ol* olivine, *Plag* plagioclase, *Opx* orthopyroxene, *Cpx* clinopyroxene, *Sp* spinel, *Mt* magnetite, *Amph* amphibole, *qu* quench crystals (detected by SEM)

[b] Fe loss probably underestimated (see text)

[c] Apparent loss or gain of FeO (total Fe as FeO) calculated as 100*(FeOcalc - FeOstarting sample)/FeOstarting sample. FeOcalc and ΣR^2 are obtained from the mass-balance calculations.

[d] Analyzed by SIMS

[e] Estimated using the by difference method

[f] Analyzed by Karl–Fischer titration

Table 4 Experimental compositions

Charge	Phase	SiO_2	TiO_2	Al_2O_3	Cr_2O_3	FeO_t	MnO	MgO	CaO	Na_2O	K_2O	Total[a]	mol%
Run 0, 1 bar, 1,400°C, Air, 2 × 3 h, Pt capsules													
STV301	Gl(41[b])	47.8(4[c])	1.10(3)	15.6(2)	0.10(1)	9.12(17)	0.17(3)	12.1(1)	11.2(1)	2.31(7)	0. 5(2)	98.3	Mg#89.0
STV315	Gl(10)	52.0(3)	0.78(8)	17.1(1)	0.02(4)	8.54(31)	0.16(9)	7.74(11)	10.7(2)	2.62(12)	0.34(5)	98.7	Mg#84.4
Run 4, 4,002 bars, 1,050°C, fH_2 = 12.6 bars, 23 h, XNi = 0.46, Au capsules													
STV301													
4-1	Gl(5)	49.4(2)	1.29(8)	18.9(1)	0.01(1)	8.31(25)	0.16(5)	6.40(16)	12.3(2)	2.60(13)	0.59(3)	90.1	Mg#64.6
	Ol(10)	39.5(2)	0.05(5)	0.04(2)	0.03(3)	12.8(11)	0.29(8)	46.3(8)	0.20(4)	0.01(2)	0.00(1)	99.2	Fo86.6
	Cpx(6)	48.1(8)	0.85(9)	5.94(83)	0.20(13)	6.15(58)	0.12(11)	15.0(6)	22.0(4)	0.30(12)	0.03(3)	98.7	En46Wo49
	Sp(3)	0.31(28)	2.62(46)	23.6(5)	17.3(3)	40.4(12)	0.16(3)	10.9(3)	0.16(9)	0.04(5)	0.01(1)	95.5	Cr#32.9
4-2	Gl(5)	50.2(3)	1.41(9)	20.7(4)	0.03(6)	8.14(22)	0.15(4)	5.19(39)	10.5(4)	3.00(14)	0.67(8)	91.7	Mg#59.1
	Ol(6)	39.1(2)	0.01(2)	0.07(9)	0.00(0)	15.5(12)	0.27(2)	43.7(10)	0.23(6)	0.01(2)	0.02(2)	98.9	Fo83.4
	Cpx(4)	47.5(7)	0.84(16)	6.47(45)	0.12(6)	7.07(25)	0.14(8)	15.2(7)	21.2(6)	0.34(9)	0.01(3)	98.9	En47Wo47
	Sp(2)	0.20(11)	2.27(6)	25.4(1)	15.4(1)	42.0(3)	0.12(5)	9.70(25)	0.19(5)	0.07(1)	0.02(3)	95.3	Cr#28.9
4-3	Gl(8)	51.9(6)	1.51(9)	21.0(4)	0.03(5)	7.85(46)	0.16(12)	3.86(52)	9.11(50)	3.76(16)	0.85(16)	92.1	Mg#52.2
	Ol(7)	38.8(3)	0.07(4)	0.06(8)	0.05(8)	18.4(5)	0.30(14)	41.5(2)	0.20(4)	0.03(4)	0.02(2)	99.4	Fo80.0
	Cpx(9)	48.6(4)	0.88(12)	6.55(31)	0.12(6)	7.19(40)	0.17(3)	14.9(5)	20.4(3)	0.38(4)	0.02(3)	99.3	En46Wo45
	Plag(3)	45.7(1)	0.06(7)	33.1(2)	0.00(0)	0.68(11)	0.03(5)	0.14(3)	17.4(2)	1.60(10)	0.07(3)	98.8	An85Or0
	Sp(3)	0.22(12)	1.66(27)	24.1(61)	17.6(25)	41.2(52)	0.08(6)	9.93(12)	0.19(3)	0.03(2)	0.02(1)	95.0	Cr#32.8
STV315													
4-4	Gl(8)	53.3(5)	0.90(4)	18.3(1)	0.03(4)	7.84(24)	0.20(10)	5.82(14)	10.6(3)	2.60(10)	0.36(5)	91.4	Mg#62.6
	Ol(3)	40.5(1)	0.03(3)	0.03(3)	0.03(5)	14.3(10)	0.32(5)	44.2(6)	0.17(10)	0.01(1)	0.02(1)	99.7	Fo84.6
	Cpx(5)	48.8(9)	0.69(15)	6.3(12)	0.50(17)	6.77(9)	0.13(8)	14.1(8)	21.4(11)	0.36(8)	0.02(2)	99.1	En44Wo47
4-5	Gl(6)	53.9(2)	1.00(5)	19.1(2)	0.02(5)	8.17(31)	0.16(12)	4.96(16)	9.32(14)	2.96(17)	0.46(5)	93.2	Mg#56.9

Charge	Phase	SiO_2	TiO_2	Al_2O_3	Cr_2O_3	FeO_t	MnO	MgO	CaO	Na_2O	K_2O	Total[a]	mol%
	Ol(2)	39.4(2)	0.05(7)	0.06(2)	0.07(2)	18.6(2)	0.29(4)	40.4(4)	0.26(3)	0.00(0)	0.00(0)	99.2	Fo79.5
	Cpx(6)	48.2(10)	0.63(4)	6.50(34)	0.30(21)	7.84(64)	0.23(9)	15.0(2)	20.0(4)	0.37(5)	0.03(3)	99.1	En46Wo45
	Plag(1)	47.8	0.01	31.8	0.05	1.15	0.00	0.45	16.8	1.68	0.09	99.9	An84Or0
4-6	Gl(2)	56.5(5)	1.19(2)	19.2(2)	0.00(0)	8.43(2)	0.15(4)	3.61(4)	7.36(42)	3.06(0)	0.53(1)	95.8	Mg#46.7
	Ol(5)	37.7(4)	0.02(2)	0.05(6)	0.00(0)	21.7(4)	0.37(9)	38.9(2)	0.26(6)	0.03(2)	0.00(0)	99.1	Fo76.1
	Cpx(4)	49.0(2)	0.81(21)	6.11(115)	0.23(6)	8.58(55)	0.14(11)	14.4(10)	19.2(8)	0.47(8)	0.06(5)	98.9	En45Wo43
	Opx(6)	51.8(5)	0.32(14)	4.66(89)	0.29(8)	13.9(4)	0.38(9)	25.6(132)	2.22(43)	0.07(8)	0.03(4)	99.3	En74Wo5
	Plag(1)	48.1	0.00	32.6	0.00	0.79	0.05	0.11	16.5	2.18	0.06	100.3	An80Or0
Run 3, 4,015 bars, 1,092°C, fH_2 = 13.2 bars, 22,5 h, XNi = 0.45, AgPd capsules													
STV301													
3-1	Gl(7)	49.6(3)	1.19(7)	17.5(2)	0.05(5)	8.26(17)	0.22(8)	7.49(18)	12.8(2)	2.38(11)	0.57(2)	92.2	Mg#67.6
	Ol(14)	39.8(5)	0.03(4)	0.12(13)	0.10(11)	12.8(3)	0.17(8)	46.0(5)	0.30(4)	0.02(2)	0.01(1)	99.3	Fo86.5
	Sp(2)	0.19(3)	1.59(8)	23.1(1)	16.7(6)	41.3(6)	0.00(0)	11.40(4)	0.29(1)	0.00(0)	0.02(3)	94.6	Cr#32.6
3-2	Gl(7)	50.0(4)	1.38(5)	19.4(1)	0.02(3)	8.27(23)	0.17(12)	6.10(12)	11.1(2)	2.87(6)	0.67(6)	93.4	Mg#62.0
	Ol(2)	40.0(1)	0.00(0)	0.09(1)	0.00(0)	14.5(9)	0.24(9)	43.4(3)	0.29(2)	0.00(0)	0.02(2)	98.5	Fo84.2
	Cpx(7)	47.1(10)	1.20(33)	8.32(113)	0.26(16)	6.59(48)	0.13(13)	14.1(9)	21.2(4)	0.34(3)	0.02(2)	99.2	En44Wo48
	Sp(2)	0.25(1)	2.43(13)	25.8(3)	18.5(1)	36.2(16)	0.21(2)	13.0(3)	0.22(4)	0.01(1)	0(0)	96.6	Cr#32.4
3-3	Gl[d]	53.5	2.00	18.3	0.00	8.62	0.00	4.54	7.73	4.00	1.27	94.9	Mg#52.9
	Ol(5)	38.8(5)	0.08(7)	0.17(18)	0.02(3)	18.2(3)	0.26(8)	41.4(3)	0.38(6)	0.02(3)	0.00(0)	99.3	Fo80.2
	Cpx(3)	47.8(5)	1.16(2)	7.47(60)	0.42(9)	6.70(13)	0.14(17)	13.5(9)	21.1(9)	0.51(19)	0.04(5)	98.7	En43Wo48
	Plag(8)	48.5(6)	0.14(7)	31.1(4)	0.02(4)	0.97(13)	0.09(9)	0.33(7)	15.6(6)	2.51(28)	0.15(7)	99.4	An77Or1
STV315													
3-5	Gl(7)	53.0(1)	0.81(9)	17.7(13)	0.02(1)	7.79(31)	0.15(11)	6.73(11)	10.9(2)	2.53(16)	0.37(3)	92.4	Mg#66.0
	Ol(6)	39.8(2)	0.01(2)	0.04(2)	0.06(8)	14.6(2)	0.2(6)	44.3(4)	0.24(7)	0(0)	0.03(4)	99.2	Fo84.4
3-6	Gl(3)	54.6(1)	1.22(1)	17.7(1)	0.06(4)	9.26(17)	0.18(5)	4.59(15)	8.81(15)	2.90(18)	0.67(6)	93.7	Mg#51.9

Charge	Phase	SiO_2	TiO_2	Al_2O_3	Cr_2O_3	FeO_t	MnO	MgO	CaO	Na_2O	K_2O	Total[a]	mol%
	Ol(5)	37.5(6)	0.03(2)	0.07(9)	0.03(4)	22.3(4)	0.34(12)	39.0(4)	0.30(9)	0.03(3)	0.02(2)	99.6	Fo75.7
	Cpx(4)	50.0(9)	0.67(13)	5.10(69)	0.21(2)	8.72(38)	0.11(13)	15.5(7)	18.7(8)	0.31(4)	0.01(3)	99.3	En47Wo40
	Plag(1)	50.4	0.07	30.6	0.05	0.84	0.08	0.28	14.8	3.00	0.10	100.2	An73Or1
	Opx(5)	52.8(8)	0.24(8)	3.98(111)	0.14(8)	12.6(4)	0.19(14)	26.6(9)	2.41(27)	0.10(8)	0.01(1)	99.1	En75Wo5
Run 6, 4,147 bars, 1,155° C, fH_2= 14.0 bars, 13 h, XNi = 0.43, AgPd capsules													
STV301													
6-1	Gl(14)	49.3(7)	1.25(9)	17.4(2)	0.06(5)	8.20(21)	0.15(8)	7.82(24)	12.5(2)	2.66(10)	0.58(3)	93.5	Mg#68.1
	Ol(5)	39.7(3)	0.01(2)	0.22(14)	0.05(5)	13.3(6)	0.24(11)	45.8(4)	0.35(11)	0.02(3)	0.01(2)	99.7	Fo86.0
	Sp(2)	0.79(10)	0.86(0)	36.8(3)	25.2(3)	19.3(5)	0.18(13)	15.7(3)	0.31(7)	0.01(1)	0.00(0)	99.1	Cr#31.5
6-2	Gl(6)	49.7(4)	1.79(10)	17.1(9)	0.03(5)	9.82(70)	0.12(8)	6.24(48)	11.1(5)	3.18(20)	0.96(7)	96.8	Mg#56.6
	Ol(13)	39.1(4)	0.05(5)	0.19(18)	0.05(6)	17.1(5)	0.18(8)	42.6(5)	0.43(10)	0.03(3)	0.01(2)	99.7	Fo81.7
	Cpx(7)	48.2(5)	0.94(10)	7.29(61)	0.51(19)	6.90(71)	0.14(11)	14.7(3)	19.8(6)	0.48(8)	0.06(5)	99.0	En46Wo45
	Plag(2)	49.9(3)	0.11(6)	29.9(6)	0.03(4)	0.79(1)	0.12(0)	0.41(8)	14.4(3)	3.23(8)	0.24(4)	99.1	An70Or1
STV315													
6-4	Gl(5)	52.3(5)	0.83(8)	17.1(2)	0.04(4)	8.16(18)	0.19(8)	7.67(12)	10.8(3)	2.50(8)	0.39(4)	94.9	Mg#67.1
6-5	Gl(4)	52.6(3)	1.14(8)	16.6(1)	0.04(7)	9.6(2)	0.3(1)	6.54(6)	10.0(2)	2.72(9)	0.49(9)	97.1	Mg#58.1
	Opx(6)	53.6(5)	0.25(5)	2.97(35)	0.28(10)	11.2(2)	0.26(11)	27.9(5)	2.63(19)	0.05(3)	0.01(1)	99.1	En78Wo5
	Cpx(5)	51.8(4)	0.44(7)	4.92(81)	0.18(7)	8.38(65)	0.20(5)	18.2(81)	14.7(13)	0.42(12)	0.06(5)	99.3	En54Wo32
	Plag(5)	50.7(4)	0.06(5)	29.8(5)	0.04(5)	0.83(17)	0.04(4)	0.44(20)	13.9(3)	3.36(12)	0.10(2)	99.3	An69Or1
Run 7, 4204 bars, 1198° C, fH_2 = 1.7 bars, 25 h, XNi = 0.12, AgPd capsules													
STV301													
7-2	Gl(5)	48.7(2)	1.11(7)	15.9(2)	0.02(5)	8.89(18)	0.12(6)	10.8(3)	11.7(2)	2.29(10)	0.52(4)	92.8	Mg#78.0
	Ol(2)	42.0(1)	0(0)	0.17(20)	0.01(1)	8.97(30)	0.14(11)	48.3(1)	0.28(3)	0.02(3)	0.02(1)	99.9	Fo90.5
	Sp(1)	0.33	0.64	25.0	29.3	25.4	0.05	15.6	0.22	0	0.03	96.6	Cr#44.0
7-3	Gl(5)	49.0(2)	1.24(6)	16.8(2)	0.02(4)	8.51(29)	0.18(8)	8.83(19)	12.3(1)	2.47(12)	0.60(4)	96.1	Mg#72.9

Charge	Phase	SiO_2	TiO_2	Al_2O_3	Cr_2O_3	FeO_t	MnO	MgO	CaO	Na_2O	K_2O	Total[a]	mol%
	Ol(1)	41.7	0.03	0.08	0.17	11.6	0.14	46.9	0.25	0(0)	0.02	100.9	Fo87.8
	Sp(1)	0.23	0.54	35.4	26.1	20.5	0.24	16.5	0.38	0	0	99.9	Cr#33.1
STV315													
7-4	Gl(4)	52.8(3)	0.79(2)	16.8(3)	0.04(7)	8.23(39)	0.09(6)	7.73(7)	10.70(7)	2.40(20)	0.36(5)	93.3	Mg#73.3
7-5	Gl(4)	52.6(5)	0.77(5)	17.2(1)	0.01(1)	8.25(22)	0.17(5)	7.61(6)	10.5(2)	2.60(21)	0.40(3)	95.9	Mg#71.3
7-6	Gl(4)	52.8(5)	0.76(5)	17.1(1)	0.06(1)	7.96(22)	0.19(5)	7.62(6)	10.5(2)	2.62(21)	0.40(3)	97.5	Mg#70.0
Run 1, 9,577 bars, 1,044°C, fH_2 = 6.0 bars, 17 h, XNi = 0.15													
STV301													
1-9	Gl(5)	64.5(6)	0.36(5)	22.6(22)	0.07(8)	0.75(13)	0.00(1)	0.56(11)	8.07(24)	2.15(25)	0.88(3)	84.5	Mg#65.7
	Amph(10)	42.7(5)	0.88(11)	12.8(2)	0.11(10)	7.07(47)	0.12(10)	16.9(4)	11.9(2)	2.19(9)	0.43(4)	95.1	Mg=0.809
	Cpx(3)	48.9(6)	0.54(3)	6.26(34)	0.08(2)	6.39(11)	0.19(7)	14.2(2)	21.4(2)	0.42(4)	0.03(4)	98.7	En44Wo48
	Mt(3)	0.21(9)	7.3(2)	3.08(14)	0.6(17)	71.3(4)	1.0(2)	3.71(7)	0.32(13)	0(0)	0.01(2)	87.6	Cr#11.8
STV315													
1-5	Gl(3)	64.4(4)	0.23(5)	22.1(1)	0.02(5)	0.55(9)	0.01(1)	0.53(4)	8.11(4)	3.18(8)	0.86(13)	84.0	Mg#71.9
	Amph(8)	43.3(5)	0.84(11)	12.7(4)	0.08(9)	6.79(78)	0.10(10)	17.1(2)	11.9(3)	2.14(11)	0.44(6)	95.4	Mg#=0.818
	Cpx(1)	48.6	0.49	6.90	0.03	6.67	0.12	14.5	21.3	0.41	0.04	99.1	En45Wo47
	Mt(3)	0.24(24)	7.49(30)	3.03(7)	0.56(17)	72.9(5)	0.76(22)	3.88(17)	0.31(4)	0.01(2)	0.02(2)	89.2	Cr#11.3

Gl glass, *Ol* olivine, *Plag* plagioclase, *Opx* orthopyroxene, *Cpx* clinopyroxene, *Sp* Cr-Al spinel, *Mt* magnetite, *Amph* amphibole
[a]Glass analyses normalised to 100% anhydrous, with all Fe as FeO. Unnormalized total is reported
[b]Number of microprobe analyses
[c]One standard deviation in terms of least unit cited
[d]Composition estimated
Mg# of glass calculated as at. 100*MgO/(MgO + FeO). FeO is determined from the electron microprobe analysis of the glass using the expression of Kress and Carmichael (*1991*) and P-T-fO_2 data from Table 3. Mg# of STV301 and STV315 starting glasses are calculated at 1 bar, 1,400°C and log fO_2 = −0.69 (air). Mg# of amphibole calculated as at. MgO/(MgO + FeO_{total}). Fo = 100*at. Mg/(Mg + Fe) in olivine. Cr# = 100*at. Cr/(Cr + Al) in spinel. En = 100*at. Mg/(Mg + Fe + Ca), Wo = 100*at. Ca/(Mg + Fe + Ca) in pyroxene, calculated with Fe = Fe^{2+} (Lindsley *1983*). An = 100*at. Ca/(Ca + Na + K), Or = 100*at. K/(Ca + Na + K) in plagioclase

Table 5 Calibration, formulation and parameters for the Al_2O_3 in melt hygrometer

Al_2O_3 = A + B/(T^C) + D*H_2O + E*SiO_2 + F*CaO + G*MgO + H*Na_2O + I*K_2O								
SiO_2, Al_2O_3, CaO, MgO, Na_2O and K_2O in wt% (from glass major element composition normalized to 100% volatile-free), H_2O in wt%, T in °C								
A	**B**	**C**	**D**	**E**	**F**	**G**	**H**	**I**
81.2265	−362.5553	0.3565	0.7632	−0.4757	−0.3524	−0.9902	−0.6634	−0.1160